



Universiteit Gent
Faculteit Wetenschappen
Vakgroep Fysica en Sterrenkunde

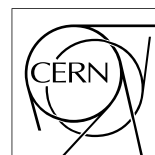
2 No title yet

3 No sub-title neither, obviously...

4 Alexis Fagot



Thesis to obtain the degree of
Doctor of Philosophy in Physics
Academic years 2012-2017





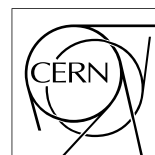
Universiteit Gent
Faculteit Wetenschappen
Vakgroep Fysica en Sterrenkunde

7
8 Promotoren: Dr. Michael Tytgat
Prof. Dr. Dirk Ryckbosch

9
10 Universiteit Gent
11 Faculteit Wetenschappen
12
13 Vakgroep Fysica en Sterrenkunde
14 Proeftuinstraat 86, B-9000 Gent, België
15 Tel.: +32 9 264.65.28
16 Fax.: +32 9 264.66.97



Thesis to obtain the degree of
Doctor of Philosophy in Physics
Academic years 2012-2017



Acknowledgements

19 Ici on remerciera tous les gens que j'ai pu croiser durant cette aventure et qui m'ont
20 permis de passer un bon moment

21 *Gent, ici la super date de la mort qui tue de la fin d'écriture*
22 *Alexis Fagot*

Table of Contents

24	Acknowledgements	i
25	Nederlandse samenvatting	xvii
26	English summary	xix
27	1 Introduction	1-1
28	1.1 A story of High Energy Physics	1-1
29	1.2 Organisation of this study	1-1
30	2 Investigating the TeV scale	2-1
31	2.1 The Standard Model of Particle Physics	2-1
32	2.2 The Large Hadron Collider and the Compact Muon Solenoid . . .	2-1
33	2.3 Muon Phase-II Upgrade	2-1
34	3 Amplification processes in gaseous detectors	3-1
35	3.1 Signal formation	3-1
36	3.2 Gas transport parameters	3-1
37	4 Resistive Plate Chambers	4-1
38	4.1 Principle	4-1
39	4.2 Rate capability of Resistive Plate Chambers	4-1
40	4.3 High time resolution	4-1
41	4.4 Resistive Plate Chambers at CMS	4-1
42	4.4.1 Overview	4-1
43	4.4.2 The present RPC system	4-2
44	4.4.3 Pulse processing of CMS RPCs	4-3
45	5 Longevity studies and Consolidation of the present CMS RPC subsys-	5-1
46	tem	
47	5.1 Testing detectors under extreme conditions	5-1
48	5.1.1 The Gamma Irradiation Facilities	5-3
49	5.1.1.1 GIF	5-3
50	5.1.1.2 GIF++	5-5
51	5.2 Preliminary tests at GIF	5-8
52	5.2.1 Resistive Plate Chamber test setup	5-8

53	5.2.2	Data Acquisition	5-10
54	5.2.3	Geometrical acceptance of the setup layout to cosmic muons	5-10
55	5.2.3.1	Description of the simulation layout	5-11
56	5.2.3.2	Simulation procedure	5-13
57	5.2.3.3	Results	5-14
58	5.2.4	Photon flux at GIF	5-15
59	5.2.4.1	Expectations from simulations	5-15
60	5.2.4.2	Dose measurements	5-19
61	5.2.5	Results and discussions	5-20
62	5.3	Longevity tests at GIF++	5-21
63	5.3.1	Description of the Data Acquisition	5-25
64	5.3.2	RPC current, environmental and operation parameter mon-	
65		itoring	5-26
66	5.3.3	Measurement procedure	5-27
67	5.3.4	Longevity studies results	5-27
68	6	Investigation on high rate RPCs	6-1
69	6.1	Rate limitations and ageing of RPCs	6-1
70	6.1.1	Low resistivity electrodes	6-1
71	6.1.2	Low noise front-end electronics	6-1
72	6.2	Construction of prototypes	6-1
73	6.3	Results and discussions	6-1
74	7	Conclusions and outlooks	7-1
75	7.1	Conclusions	7-1
76	7.2	Outlooks	7-1
77	A	A data acquisition software for CAEN VME TDCs	A-1
78	A.1	Description of the setup	A-1
79	A.2	Data read-out	A-3
80	A.2.1	V1190A TDCs	A-3
81	A.2.2	V1718 USB Bridge	A-6
82	A.2.3	DataReader	A-6
83	A.2.4	DAQ algorithm overview	A-9
84	A.3	Software export	A-9
85	B	Details on the online analysis package	B-1
86	B.1	Introduction	B-1
87	C	Structure of the hybrid simulation software	C-1
88	C.1	Introduction	C-1

List of Figures

90	2.1	Absorbed dose in the CMS cavern after an integrated luminosity	
91		of 3000 fb. R is the transverse distance from the beamline and Z is	
92		the distance along the beamline from the Interaction Point at Z=0.	2-2
93	2.2	A quadrant of the muon system, showing DTs (yellow), RPCs	
94		(light blue), and CSCs (green). The locations of new forward	
95		muon detectors for Phase-II are contained within the dashed box	
96		and indicated in red for GEM stations (ME0, GE1/1, and GE2/1)	
97		and dark blue for improved RPC (iRPC) stations (RE3/1 and RE4/1).	2-3
98	2.3	RMS of the multiple scattering displacement as a function of muon	
99		p_T for the proposed forward muon stations. All of the electromag-	
100		netic processes such as bremsstrahlung and magnetic field effect	
101		are included in the simulation.	2-4
102	4.1	Signals from the RPC strips are shaped by the FEE described on	
103		Figure 4.1a. Output LVDS signals are then read-out by a TDC	
104		module connected to a computer or converted into NIM and sent	
105		to scalers. Figure 4.1b describes how these converted signals are	
106		put in coincidence with the trigger.	4-4
107	4.2	Description of the principle of a CFD. A comparison of threshold	
108		triggering (left) and constant fraction triggering (right) is shown	
109		in Figure 4.2a. Constant fraction triggering is obtained thanks to	
110		zero-crossing technique as explained in Figure 4.2b. The signal	
111		arriving at the input of the CFD is split into three components. A	
112		first one is delayed and connected to the inverting input of a first	
113		comparator. A second component is connected to the noninverting	
114		input of this first comparator. A third component is connected to	
115		the noninverting input of another comparator along with a thresh-	
116		old value connected to the inverting input. Finally, the output of	
117		both comparators is fed through an AND gate.	4-5
118	5.1	(5.1a) Extrapolation from 2016 data of single hit rate per unit area	
119		in the barrel region. (5.1b) Extrapolation from 2016 data of single	
120		hit rate per unit area in the endcap region.	5-2

121	5.2	Background Fluka simulation compared to 2016 Data at $L = 10^{34} \text{cm}^{-2} \cdot \text{s}^{-1}$	
122		in the fourth endcap disk region. A mismatch in between simula-	
123		tion and data can be observed. [To be understood.]	5-3
124	5.3	Layout of the test beam zone called X5c GIF at CERN. Photons	
125		from the radioactive source produce a sustained high rate of ran-	
126		dom hits over the whole area. The zone is surrounded by 8 m high	
127		and 80 cm thick concrete walls. Access is possible through three	
128		entry points. Two access doors for personnel and one large gate	
129		for material. A crane allows installation of heavy equipment in the	
130		area.	5-4
131	5.4	^{137}Cs decays by β^- emission to the ground state of ^{137}Ba (BR =	
132		5.64%) and via the 662 keV isomeric level of ^{137}Ba (BR = 94.36%)	
133		whose half-life is 2.55 min.	5-5
134	5.5	Floor plan of the GIF++ facility. When the facility downstream of	
135		the GIF++ takes electron beam, a beam pipe is installed along the	
136		beam line (z-axis). The irradiator can be displaced laterally (its	
137		center moves from $x = 0.65$ m to 2.15 m), to increase the distance	
138		to the beam pipe.	5-6
139	5.6	Simulated unattenuated current of photons in the xz plane (Fig-	
140		ure 5.6a) and yz plane (Figure 5.6b) through the source at $x = 0.65$ m	
141		and $y = 0$ m. With angular correction filters, the current of 662 keV	
142		photons is made uniform in xy planes.	5-7
143	5.7	Description of the RPC setup. Dimensions are given in mm. A	
144		tent containing RPCs is placed at 1720 mm from the source con-	
145		tainer. The source is situated in the center of the container. RE-	
146		4-2-BARC-161 chamber is 160 mm inside the tent. This way, the	
147		distance between the source and the chambers plan is 2060 mm.	
148		Figure 5.7a provides a side view of the setup in the xz plane while	
149		Figure 5.7b shows a top view in the yz plane.	5-8
150	5.8	RE-4-2-BARC-161 chamber is inside the tent as described in Fig-	
151		ure 5.7. In the top right, the two scintillators used as trigger can	
152		be seen. This trigger system has an inclination of 10° relative	
153		to horizontal and is placed above half-partition B2 of the RPCs.	
154		PMT electronics are shielded thanks to lead blocks placed in order	
155		to protect them without stopping photons from going through the	
156		scintillators and the chamber.	5-9

157	5.9	Hit distributions over all 3 parttions of RE-4-2-BARC-161 cham-	
158		ber is showed on these plots. Top, middle and bottom figures re-	
159		spectively correspond to partitions A, B, and C. These plots show	
160		that some events still occur in other half-partitions than B2, which	
161		corresponds to strips 49 to 64, in front of which the trigger is	
162		placed, contributing to the inefficiency of detection of cosmic muons.	
163		In the case of partitions A and C, the very low amount of data can	
164		be interpreted as noise. On the other hand, it is clear that a lit-	
165		tle portion of muons reach the half-partition B1, corresponding to	
166		strips 33 to 48.	5-10
167	5.10	Results are derived from data taken on half-partition B2 only. On	
168		the 18 th of June 2014, data has been taken on chamber RE-2-	
169		BARC-161 at building 904 (Prevessin Site) with cosmic muons	
170		providing us a reference efficiency plateau of $(97.54 \pm 0.15)\%$ rep-	
171		resented by a black curve. A similar measurement has been done	
172		at GIF on the 21 st of July with the same chamber giving a plateau	
173		of $(78.52 \pm 0.94)\%$ represented by a red curve.	5-11
174	5.11	Representation of the layout used for the simulations of the test	
175		setup. The RPC is represented as a yellow trapezoid while the two	
176		scintillators as blue cuboids looking at the sky. A green plane cor-	
177		responds to the muon generation plane within the simulation. Fig-	
178		ure 5.7a shows a global view of the simulated setup. Figure 5.7b	
179		shows a zommed view that allows to see the 2 scintillators as well	
180		as the full RPC plane.	5-12
181	5.12	γ flux $F(D)$ is plot using values from table 5.1. As expected, the	
182		plot shows similar attenuation behaviours with increasing distance	
183		for each absorption factors.	5-15
184	5.13	Figure 5.13a shows the linear approximation fit done via formu-	
185		lae 5.7 on data from table 5.2. Figure 5.13b shows a comparison	
186		of this model with the simulated flux using a and b given in fig-	
187		ure 5.13a in formulae 5.4 and the reference value $D_0 = 50cm$	
188		and the associated flux for each absorption factor F_0^{ABS} from ta-	
189		ble 5.1	5-17
190	5.14	Dose measurements has been done in a plane corresponding to the	
191		tents front side. This plan is 1900 mm away from the source. As	
192		explained in the first chapter, a lens-shaped lead filter provides a	
193		uniform photon flux in the vertical plan orthogonal to the beam	
194		direction. If the second line of measured fluxes is not taken into	
195		account because of lower values due to experimental equipments	
196		in the way between the source and the tent, the uniformity of the	
197		flux is well showed by the results.	5-19
198	5.15	5-20

199	5.16	Evolution of the maximum efficiency for RE2 (5.16a) and RE4	
200		(5.16b) chambers with increasing extrapolated γ rate per unit area	
201		at working point. Both irradiated (blue) and non irradiated (red)	
202		chambers are shown.	5-22
203	5.17	Evolution of the working point for RE2 (5.17a) and RE4 (5.17b)	
204		with increasing extrapolated γ rate per unit area at working point.	
205		Both irradiated (blue) and non irradiated (red) chambers are shown.	5-23
206	5.18	Evolution of the maximum efficiency at HL-LHC conditions, i.e.	
207		a background hit rate per unit area of 300 Hz/cm^2 , with increasing	
208		integrated charge for RE2 (5.18a) and RE4 (5.18b) detectors. Both	
209		irradiated (blue) and non irradiated (red) chambers are shown. The	
210		integrated charge for non irradiated detectors is recorded during	
211		test beam periods and stays small with respect to the charge accu-	
212		culated in irradiated chambers.	5-23
213	5.19	Comparison of the efficiency sigmoid before (triangles) and after	
214		(circles) irradiation for RE2 (5.19a) and RE4 (5.19b) detectors.	
215		Both irradiated (blue) and non irradiated (red) chambers are shown.	5-24
216	5.20	Evolution of the Bakelite resistivity for RE2 (5.20a) and RE4 (5.20b)	
217		detectors. Both irradiated (blue) and non irradiated (red) chambers	
218		are shown.	5-24
219	5.21	Evolution of the noise rate per unit area for the irradiated chamber	
220		RE2-2-BARC-9 only.	5-25
221	A.1	(A.1a) View of the front panel of a V1190A TDC module [8].	
222		(A.1b) View of the front panel of a V1718 Bridge module [V1718MUT].	
223		(A.1c) View of the front panel of a 6U 6021 VME crate [6U6000MUT].	A-2
224	A.2	Module V1190A <i>Trigger Matching Mode</i> timing diagram [8]. . . .	A-3

List of Tables

226	5.1	Total photon flux ($E\gamma \leq 662$ keV) with statistical error predicted	
227		considering a ^{137}Cs activity of 740 GBq at different values of the	
228		distance D to the source along the x-axis of irradiation field [6]. . .	5-15
229	5.2	Correction factor c is computed thanks to formulae 5.5 taking as	
230		reference $D_0 = 50$ cm and the associated flux F_0^{ABS} for each ab-	
231		sorption factor available in table 5.1.	5-16
232	5.3	The data at D_0 in 1997 is taken from [6]. In a second step, using	
233		Equations 5.8 and 5.9, the flux at D can be estimated in 1997.	
234		Then, taking into account the attenuation of the source activity,	
235		the flux at D can be estimated at the time of the tests in GIF in	
236		2014. Finally, assuming a sensitivity of the RPC to γ $s = 2 \cdot 10^{-3}$,	
237		an estimation of the hit rate per unit area is obtained.	5-18

238

List of Acronyms

239

List of Acronyms

240

241

242

A

243

244

AFL

Almost Full Level

245

246

247

B

248

249

BARC

Bhabha Atomic Research Centre

250

BLT

Block Transfer

251

BR

Branching Ratio

252

253

254

C

255

256

CAEN

Costruzioni Apparecchiature Elettroniche Nucleari S.p.A.

257

258

CERN

European Organization for Nuclear Research

259

CFD

Constant Fraction Discriminator

260

CMS

Compact Muon Solenoid

261

CSC

Cathode Strip Chamber

262

263

264

D

265

266

DAQ

Data Acquisition

267

DCS

Detector Control Software

268

DQM

Data Quality Monitoring

269	DT	Drift Tube
270		
271		
272	F	
273		
274	FEE	Front-End Electronics
275	FEB	Front-End Board
276		
277		
278	G	
279		
280	GE-/-	Find a good description
281	GE1/1	Find a good description
282	GE2/1	Find a good description
283	GEANT	GEometry ANd Tracking - a series of software toolkit
284		platforms developed by CERN
285	GEM	Gas Electron Multiplier
286	GIF	Gamma Irradiation Facility
287	GIF++	new Gamma Irradiation Facility
288		
289		
290	H	
291		
292	HL-LHC	High Luminosity LHC
293	HV	High Voltage
294		
295		
296	I	
297		
298	iRPC	improved RPC
299	IRQ	Interrupt Request
300		
301		
302	L	
303		
304	LHC	Large Hadron Collider
305	LS1	First Long Shutdown
306	LS3	Third Long Shutdown

307	LV	Low Voltage
308	LVDS	Low-Voltage Differential Signaling
309		
310		
311	M	
312		
313	MC	Monte Carlo
314	MCNP	Monte Carlo N-Particle
315	ME-/-	Find good description
316	ME0	Find good description
317		
318		
319	N	
320		
321	NIM	Nuclear Instrumentation Module logic signals
322		
323		
324	P	
325		
326	PMT	PhotoMultiplier Tube
327		
328		
329	R	
330		
331	RE-/-	Find a good description
332	RE2/2	Find a good description
333	RE3/1	Find a good description
334	RE3/2	Find a good description
335	RE4/1	Find a good description
336	RE4/2	Find a good description
337	RE4/3	Find a good description
338	RMS	Root Mean Square
339	ROOT	a framework for data processing born at CERN
340	RPC	Resistive Plate Chamber
341		
342		
343	S	
344		
345	SPS	Super Proton Synchrotron

346

347

348 **T**

349

350 TDC Time-to-Digital Converter

352

Nederlandse samenvatting –Summary in Dutch–

353

354 Le resume en Neerlandais (j'aurais peut-etre de apprendre la langue juste pour
355 ca...).

English summary

357 Le meme résumé mais en Anglais (on commencera par la hein!).

1

Introduction

358

359

360 **1.1 A story of High Energy Physics**

361 **1.2 Organisation of this study**

2

Investigating the TeV scale

2.1 The Standard Model of Particle Physics

2.2 The Large Hadron Collider and the Compact Muon Solenoid

2.3 Muon Phase-II Upgrade

After the more than two years lasting First Long Shutdown (LS1), the Large Hadron Collider (LHC) delivered its very first Run-II proton-proton collisions early 2015. LS1 gave the opportunity to the LHC and to the its experiments to undergo upgrades. The accelerator is now providing collisions at center-of-mass energy of 13 TeV and bunch crossing rate of 40 MHz, with a peak luminosity exceeding its design value. During the first and upcoming second LHC Long Shutdown, the Compact Muon Solenoid (CMS) detector is also undergoing a number of upgrades to maintain a high system performance [1].

From the LHC Phase-2 or High Luminosity LHC (HL-LHC) period onwards, i.e. past the Third Long Shutdown (LS3), the performance degradation due to integrated radiation as well as the average number of inelastic collisions per bunch crossing, or pileup, will rise substantially and become a major challenge for the LHC experiments, like CMS that are forced to address an upgrade program for Phase-II [2]. Simulations of the expected distribution of absorbed dose in the CMS detector under HL-LHC conditions, show in figure 5.14 that detectors placed close

to the beamline will have to withstand high irradiation, the radiation dose being of the order of a few tens of Gy.

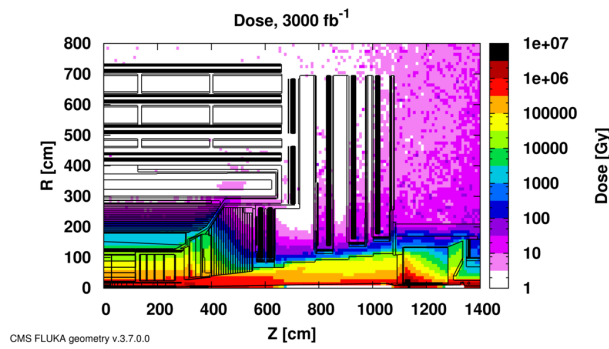


Figure 2.1: Absorbed dose in the CMS cavern after an integrated luminosity of 3000 fb. R is the transverse distance from the beamline and Z is the distance along the beamline from the Interaction Point at $Z=0$.

The measurement of small production cross-section and/or decay branching ratio processes, such as the Higgs boson coupling to charge leptons or the $B_s \rightarrow \mu^+ \mu^-$ decay, is of major interest and specific upgrades in the forward regions of the detector will be required to maximize the physics acceptance on the largest possible solid angle. To ensure proper trigger performance within the present coverage, the muon system will be completed with new chambers. In figure 2.2 one can see that the existing Cathode Strip Chambers (CSCs) will be completed by Gas Electron Multipliers (GEMs) and Resistive Plate Chambers (RPCs) in the pseudorapidity region $1.6 < |\eta| < 2.4$ to complete its redundancy as originally scheduled in the CMS Technical Proposal [3].

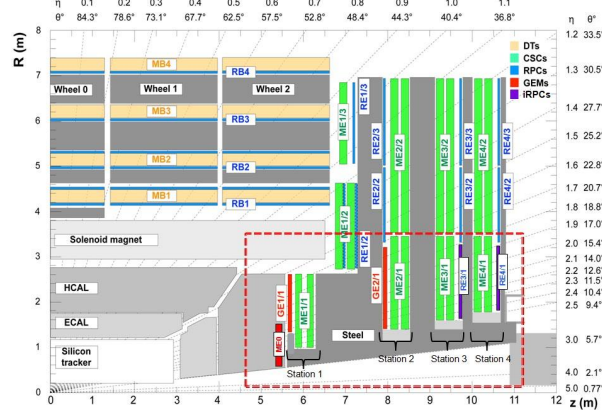


Figure 2.2: A quadrant of the muon system, showing DTs (yellow), RPCs (light blue), and CSCs (green). The locations of new forward muon detectors for Phase-II are contained within the dashed box and indicated in red for GEM stations (ME0, GE1/1, and GE2/1) and dark blue for improved RPC (iRPC) stations (RE3/1 and RE4/1).

395 RPCs are used by the CMS first level trigger for their good timing perfor-
 396 manances. Indeed, a very good bunch crossing identification can be obtained with the
 397 present CMS RPC system, given their fast response of the order of 1 ns. In order
 398 to contribute to the precision of muon momentum measurements, muon chambers
 399 should have a spatial resolution less or comparable to the contribution of multiple
 400 scattering [1]. Most of the plausible physics is covered only considering muons
 401 with $p_T < 100$ GeV thus, in order to match CMS requirements, a spatial resolu-
 402 tion of $\mathcal{O}(\text{few mm})$ the proposed new RPC stations, as shown by the simulation in
 403 figure 2.3. According to preliminary designs, RE3/1 and RE4/1 readout pitch will
 404 be comprised between 3 and 6 mm and 5 η -partitions could be considered.

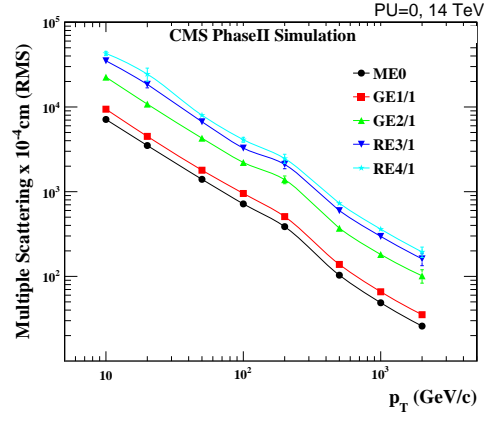


Figure 2.3: RMS of the multiple scattering displacement as a function of muon p_T for the proposed forward muon stations. All of the electromagnetic processes such as bremsstrahlung and magnetic field effect are included in the simulation.

3

405

406

Amplification processes in gaseous detectors

407

408

3.1 Signal formation

409

3.2 Gas transport parameters

4

Resistive Plate Chambers

4.1 Principle

4.2 Rate capability of Resistive Plate Chambers

4.3 High time resolution

4.4 Resistive Plate Chambers at CMS

4.4.1 Overview

The Resistive Plate Chambers (RPC) system, located in both barrel and endcap regions, provides a fast, independent muon trigger with a looser p_T threshold over a large portion of the pseudorapidity range ($|\eta| < 1.6$) [\[add reconstruction\]](#).

During High-Luminosity LHC (HL-LHC) operations the expected conditions in terms of background and pile-up will make the identification and correct P_T assignment a challenge for the Muon system. The goal of RPC upgrade is to provide additional hits to the Muon system with precise timing. All these informations will be elaborated by the trigger system in a global way enhancing the performance of the trigger in terms of efficiency and rate control. The RPC Upgrade is based on two projects: an improved Link Board System and the extension of the RPC coverage up to $|\eta| = 2.4$. [\[FIXME 2.4 or 2.5?\]](#)

The Link Board system, that will be described in section xxx, is responsible to process, synchronize and zero-suppress the signals coming from the RPC front end boards. The Link Board components have been produced between 2006 and 2007 and will be subjected to aging and failure in the long term. The upgraded Link Board system will overcome the aging problems described in section xxx and will allow for a more precise timing information to the RPC hits from 25 to 1 ns [ref section xxx].

The extension of the RPC system up to $|\eta| = 2.1$ was already planned in the CMS TDR [ref cmstdr] and staged because of budget limitations and expected background rates higher than the rate capability of the present CMS RPCs in that region. An extensive R&D program has been done in order to develop an improved RPC that fulfills the CMS requirements. Two new RPC layers in the innermost ring of stations 3 and 4 will be added with benefits to the neutron-induced background reduction and efficiency improvement for both trigger and offline reconstruction.

4.4.2 The present RPC system

The RPC system is organized in 4 stations called RB1 to RB4 in the barrel region, and RE1 to RE4 in the endcap region. The innermost barrel stations, RB1 and RB2, are instrumented with 2 layers of RPCs facing the innermost (RB1in and RB2in) and outermost (RB1out and RB2out) sides of the DT chambers. Every chamber is then divided from the read-out point of view into 2 or 3 η partitions called “rolls”. The RPC system consist of 480 barrel chambers and 576 endcap chambers. Details on the geometry are discussed in the paper [ref to geo paper].

The CMS RPC chamber is a double-gap, operated in avalanche mode to ensure reliable operation at high rates. Each RPC gap consists of two 2-mm-thick resistive High-Pressure Laminate (HPL) plates separated by a 2-mm-thick gas gap. The outer surface of the HPL plates is coated with a thin conductive graphite layer, and a voltage is applied. The RPCs are operated with a 3-component, non-flammable gas mixture consisting of 95.2% freon ($C_2H_2F_4$, known as R134a), 4.5% isobutane ($i-C_4H_{10}$), and 0.3% sulphur hexafluoride (SF_6) with a relative humidity of 40% - 50%. Readout strips are aligned in η between the 2 gas gaps. [\[Add a sentence on FEBs.\]](#)

The discriminated signals coming from the Front End boards feed via twisted cables (10 to 20 m long) the Link Board System located in UXC on the balconies around the detector. The Link System consist of the 1376 Link Boards (LBs) and the 216 Control Boards (CBs), placed in 108 Link Boxes. The Link Box is a custom crate (6U high) with 20 slots (for two CBs and eighteen LBs). The Link Box contains custom backplane to which the cables from the chambers are connected, as well as the cables providing the LBs and CBs power supply and the cables for the RPC FEBs control with use of the I2C protocol (through the CB). The

backplane itself contains only connectors (and no any other electronic devices).

The Link Board has 96 input channels (one channel corresponds to one RPC strip). The input signals are the ~ 100 ns binary pulses which are synchronous to the RPC hits, but not to the LHC clock (which drives the entire CMS electronics). Thus the first step of the FEB signals processing is synchronization, i.e. assignment of the signals to the BXes (25 ns periods). Then the data are compressed with a simple zero-suppressing algorithm (the input channels are grouped into 8 bit partitions, only the partitions with at least one nonzero bit are selected for each BX). Next, the non-empty partitions are time-multiplexed i.e. if there are more than one such partition in a given BX, they are sent one-by-one in consecutive BXes. The data from 3 neighbouring LBs are concentrated by the middle LB which contains the optical transmitter for sending them to the USC over a fiber at 1.6 Gbps.

The Control Boards provide the communication of the control software with the LBs via the FEC/CCU system. The CBs are connected into token rings, each ring consists of 12 CBs of one detector tower and a FEC mezzanine board placed on the CCS board located in the VME crate in the USC. In total, there are 18 rings in the entire Link System. The CBs also perform automatic reloading of the LB's firmware which is needed in order to avoid accumulation of the radiation induced SEUs in the LBs firmware.

Both LBs and CB are based on the Xilinx Spartan III FPGAs, the CB additionally contains radiation-tolerant (FLASH based) FPGA Actel ProAsicPlus.

The High Voltage power system is located in USC, not exposed to radiation and easily accessible for any reparation. A single HV channel powers 2 RPC chambers both in the barrel and endcap regions. The Low Voltage boards are located in UXC on the balconies and provide the voltage to the front end electronics.

4.4.3 Pulse processing of CMS RPCs

Signals induced by cosmic particle in the RPC strips are shaped by standard CMS RPC Front-End Electronics (FEE) following the scheme of Figure 4.1. On a first stage, analogic signals are amplified and then sent to the Constant Fraction Discriminator (CFD) described in Figure 4.2. At the end of the chain, 100 ns long pulses are sent in the LVDS output. These output signal are sent on one side to a V1190A Time-to-Digital Converter (TDC) module from CAEN and on the other to an OR module to count the number of detected signals. Trigger and hit coincidences are monitored using scalers. The TDC is used to store the data into ROOT files. These files are thus analysed to understand the detectors performance.

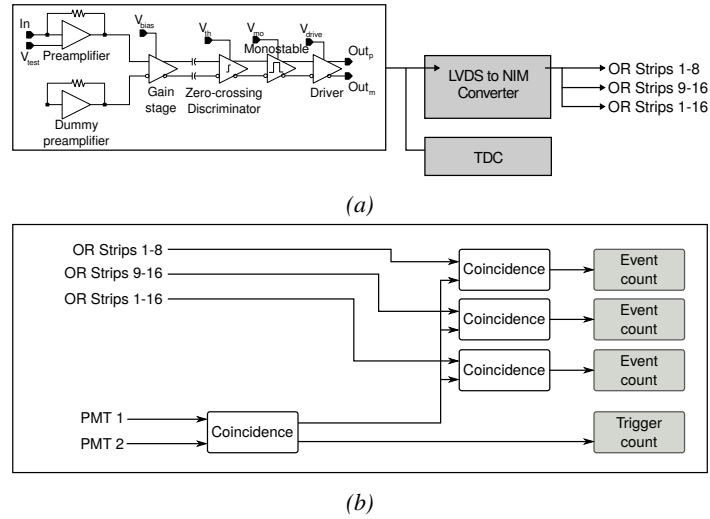


Figure 4.1: Signals from the RPC strips are shaped by the FEE described on Figure 4.1a. Output LVDS signals are then read-out by a TDC module connected to a computer or converted into NIM and sent to scalars. Figure 4.1b describes how these converted signals are put in coincidence with the trigger.

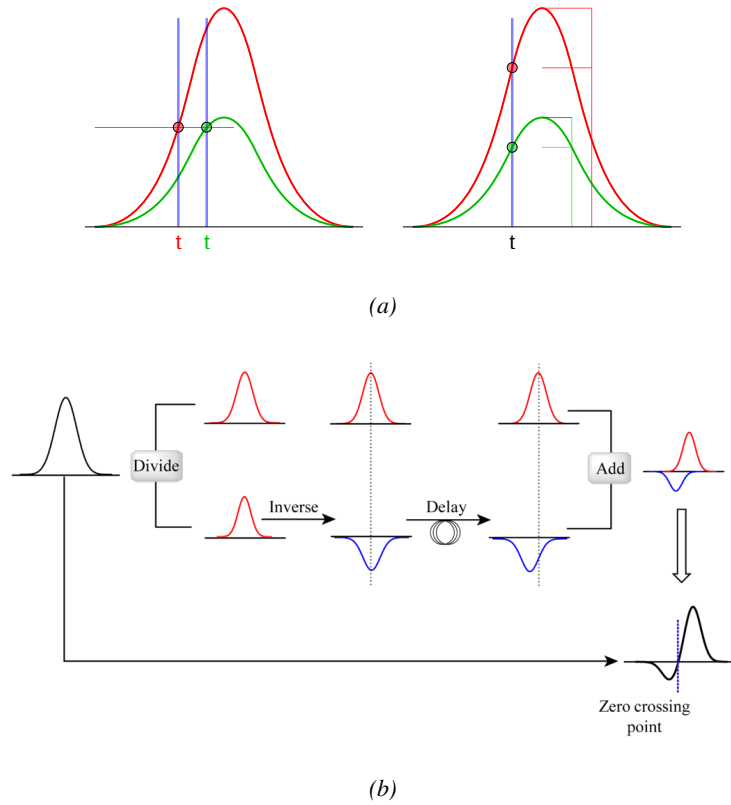


Figure 4.2: Description of the principle of a CFD. A comparison of threshold triggering (left) and constant fraction triggering (right) is shown in Figure 4.2a. Constant fraction triggering is obtained thanks to zero-crossing technique as explained in Figure 4.2b. The signal arriving at the input of the CFD is split into three components. A first one is delayed and connected to the inverting input of a first comparator. A second component is connected to the noninverting input of this first comparator. A third component is connected to the noninverting input of another comparator along with a threshold value connected to the inverting input. Finally, the output of both comparators is fed through an AND gate.

5

503

504 Longevity studies and Consolidation of 505 the present CMS RPC subsystem

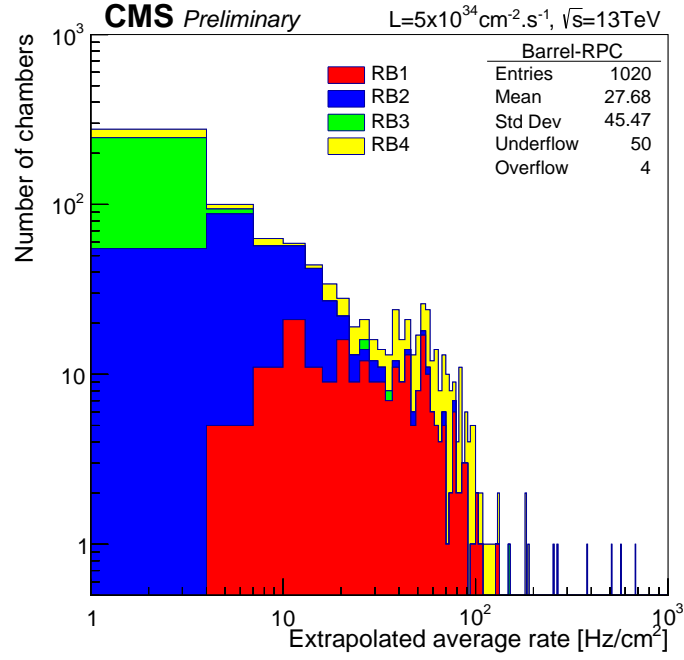
506 5.1 Testing detectors under extreme conditions

507 The upgrade from LHC to HL-LHC will increase the peak luminosity from 10^{34}
508 $\text{cm}^{-2} \text{s}^{-1}$ to reach $5 \times 10^{34} \text{cm}^{-2} \text{s}^{-1}$, increasing in the same way the total ex-
509 pected background to which the RPC system will be subjected to. Composed of
510 low energy gammas and neutrons from p - p collisions, low momentum primary
511 and secondary muons, punch-through hadrons from calorimeters, and particles pro-
512 duced in the interaction of the beams with collimators, the background will mostly
513 affect the regions of CMS that are the closest to the beam line, i.e. the RPC detec-
514 tors located in the endcaps. [\[To update.\]](#)

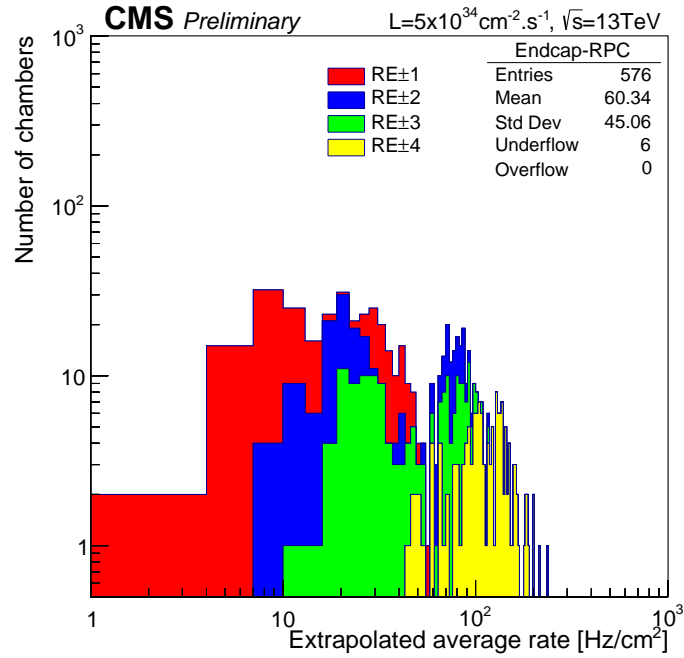
515

516 The 2016 data allowed to study the values of the background rate in all RPC
517 system. In Figure 5.1, the distribution of the chamber background hit rate per unit
518 area is shown at a luminosity of $5 \times 10^{34} \text{cm}^{-2} \cdot \text{s}^{-1}$ linearly extrapolating from
519 data collected in 2016 [\[ref mentioning the linear dependency of rate vs lumi\]](#). The
520 maximum rate per unit area at HL-LHC conditions is expected to be of the or-
521 der of $600 \text{Hz}/\text{cm}^2$ (including a safety factor 3). Nevertheless, Fluka simulations
522 have conducted in order to understand the background at HL-LHC conditions. The
523 comparison to the data has shown, in Figure 5.2, a discrepancy of a factor 2 even
524 though the order of magnitude is consistent. [\[Understand mismatch.\]](#)

525



(a)



(b)

Figure 5.1: (5.1a) Extrapolation from 2016 data of single hit rate per unit area in the barrel region. (5.1b) Extrapolation from 2016 data of single hit rate per unit area in the endcap region.

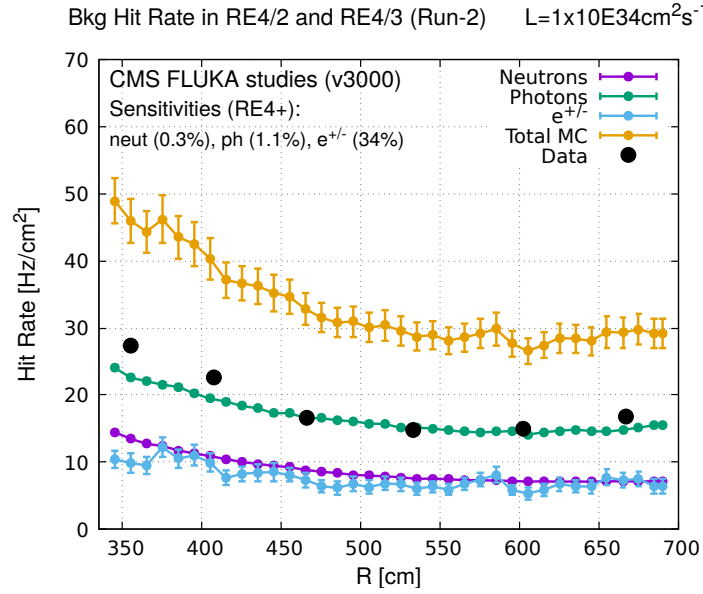


Figure 5.2: Background Fluka simulation compared to 2016 Data at $L = 10^{34} \text{cm}^{-2} \cdot \text{s}^{-1}$ in the fourth endcap disk region. A mismatch in between simulation and data can be observed. [To be understood.]

In the past, extensive long-term tests were carried out at several gamma and neutron facilities certifying the detector performance. Both full size and small prototype RPCs have been irradiated with photons up to an integrated charge of $\sim 0.05 \text{C/cm}^2$ and $\sim 0.4 \text{C/cm}^2$, respectively [4, 5]. During Run-I, the RPC system provided stable operation and excellent performance and did not show any aging effects for integrated charge of the order of 0.01C/cm^2 . Projections on currents from 2016 Data, has allowed to determine that the total integrated charge, by the end of HL-LHC, would be of the order of 1C/cm^2 (including a safety factor 3). [Corresponding figure needed.]

5.1.1 The Gamma Irradiation Facilities

5.1.1.1 GIF

Located in the SPS West Area at the downstream end of the X5 test beam, the Gamma Irradiation Facility (GIF) was a test area in which particle detectors were exposed to a particle beam in presence of an adjustable gamma background [6]. Its goal was to reproduce background conditions these detectors would suffer in their operating environment at LHC. GIF layout is shown in Figure 5.3. Gamma

photons are produced by a strong ^{137}Cs source installed in the upstream part of the zone inside a lead container. The source container includes a collimator, designed to irradiate a $6 \times 6 \text{ m}^2$ area at 5 m maximum to the source. A thin lens-shaped lead filter helps providing with a uniform outgoing flux in a vertical plane, orthogonal to the beam direction. The principal collimator hole provides a pyramidal aperture of $74^\circ \times 74^\circ$ solid angle and provides a photon flux in a pyramidal volume along the beam axis. The photon rate is controlled by further lead filters allowing the maximum rate to be limited and to vary within a range of four orders of magnitude. Particle detectors under test are then placed within the pyramidal volume in front of the source, perpendicularly to the beam line in order to profit from the homogeneous photon flux. Adjusting the background flux of photons can then be done by using the filters and choosing the position of the detectors with respect to the source.

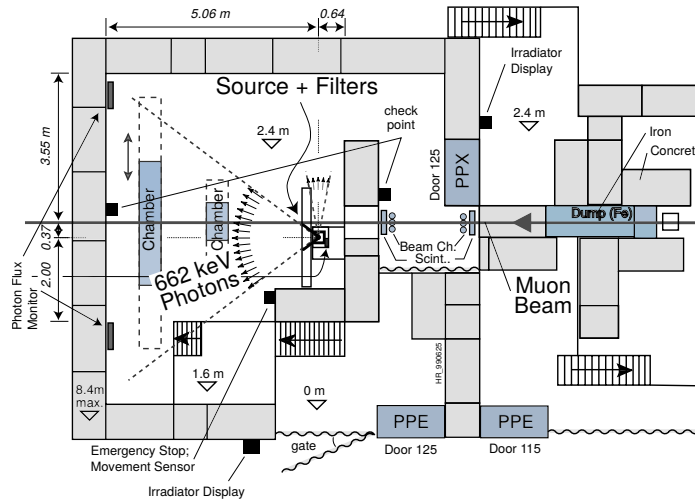


Figure 5.3: Layout of the test beam zone called X5c GIF at CERN. Photons from the radioactive source produce a sustained high rate of random hits over the whole area. The zone is surrounded by 8 m high and 80 cm thick concrete walls. Access is possible through three entry points. Two access doors for personnel and one large gate for material. A crane allows installation of heavy equipment in the area.

As described on Figure 5.4, the ^{137}Cs source emits a 662 keV photon in 85% of the decays. An activity of 740 GBq was measured on the 5th March 1997. To estimate the strength of the flux in 2014, it is necessary to consider the nuclear decay through time associated to the Cesium source whose half-life is well known ($t_{1/2} = (30.05 \pm 0.08) \text{ y}$). The GIF tests were done in between the 20th and the 31st of August 2014, i.e. at a time $t = (17.47 \pm 0.02) \text{ y}$ resulting in an attenuation

of the activity from 740 GBq in 1997 to 494 GBq in 2014.

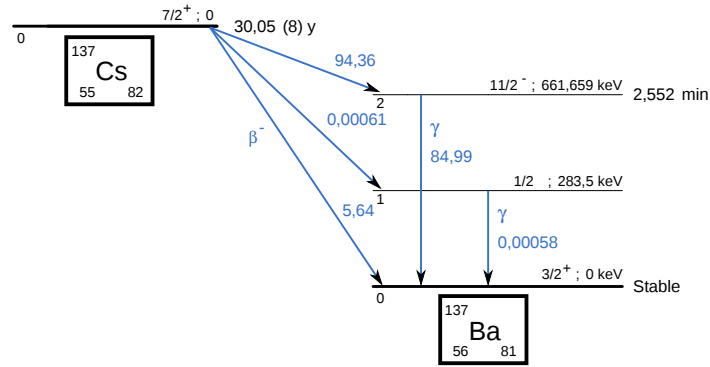


Figure 5.4: ^{137}Cs decays by β^- emission to the ground state of ^{137}Ba (BR = 5.64%) and via the 662 keV isomeric level of ^{137}Ba (BR = 94.36%) whose half-life is 2.55 min.

5.1.1.2 GIF++

The new Gamma Irradiation Facility (GIF++), located in the SPS North Area at the downstream end of the H4 test beam, has replaced its predecessor during LS1 and has been operational since spring 2015 [7]. Like GIF, GIF++ features a ^{137}Cs source of 662 keV gamma photons, their fluence being controlled with a set of filters of various attenuation factors. The source provides two separated large irradiation areas for testing several full-size muon detectors with continuous homogeneous irradiation, as presented in Figure 5.5.

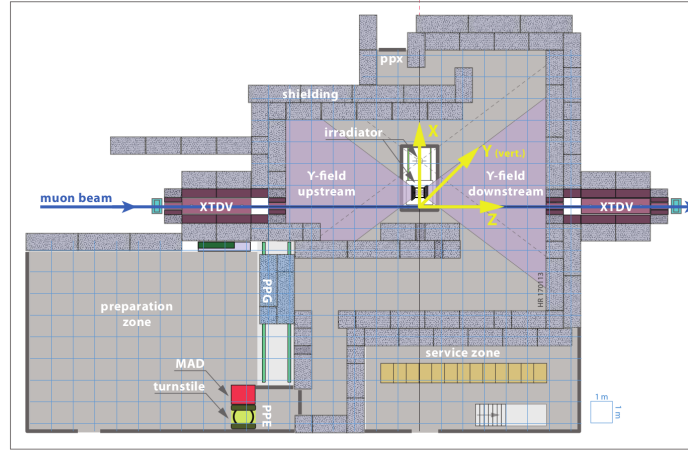


Figure 5.5: Floor plan of the GIF++ facility. When the facility downstream of the GIF++ takes electron beam, a beam pipe is installed along the beam line (z -axis). The irradiator can be displaced laterally (its center moves from $x = 0.65$ m to 2.15 m), to increase the distance to the beam pipe.

574 The source activity was measured to be about 13.5 TBq in March 2016. The
 575 photon flux being far greater than HL-LHC expectations, GIF++ provides an ex-
 576 cellent facility for accelerated aging tests of muon detectors.
 577

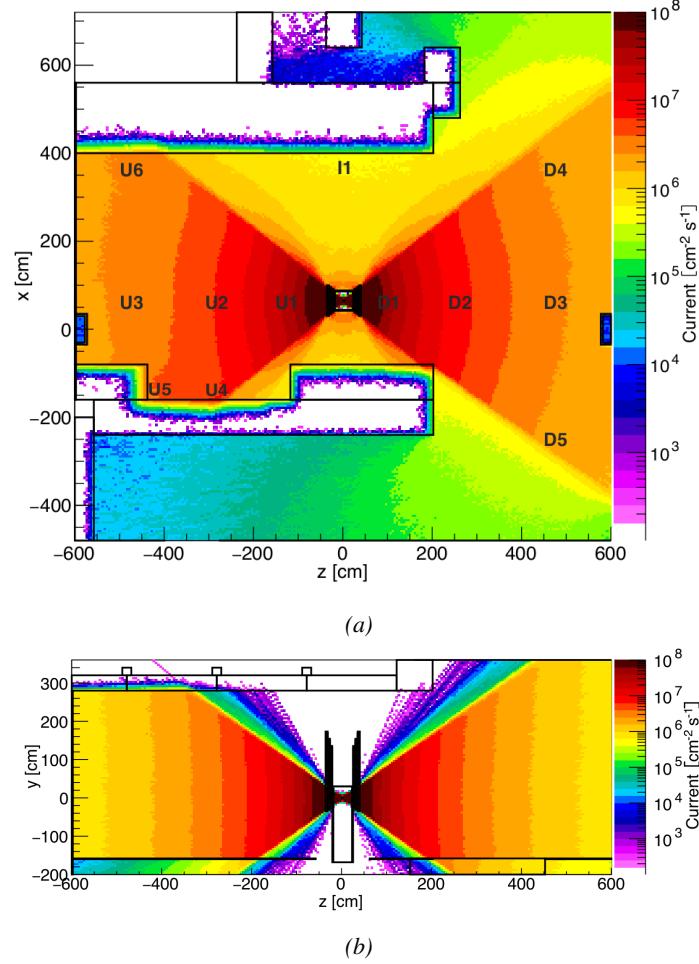


Figure 5.6: Simulated unattenuated current of photons in the xz plane (Figure 5.6a) and yz plane (Figure 5.6b) through the source at $x=0.65$ m and $y=0$ m. With angular correction filters, the current of 662 keV photons is made uniform in xy planes.

578 The source is situated in the muon beam line with the muon beam being avail-
 579 able a few times a year. The H4 beam, composed of muons with a momentum of
 580 about 150 GeV/c, passes through the GIF++ zone and is used to study the per-
 581 formance of the detectors. Its flux is of 104 particles/s/cm² focused in an area
 582 similar to 10×10 cm². Therefore, with properly adjusted filters, one can imitate
 583 the HL-LHC background and study the performance of muon detectors with their
 584 trigger/readout electronics in HL-LHC environment.

585

5.2 Preliminary tests at GIF

5.2.1 Resistive Plate Chamber test setup

During summer 2014, preliminary tests have been conducted in the GIF area on a newly produced RE4/2 chamber labelled RE-4-2-BARC-161. This chamber has been placed into a trolley covered with a tent. The position of the RPC inside the tent and of the tent related to the source is described in Figure 5.7. To test this CMS RPC, three different absorber settings were used. First of all, measurements were done with fully opened source. Then, to complete this preliminary study, the gamma flux has been attenuated from a factor 2 and a factor 5. The expected gamma flux at the level of our detector will be discussed in subsection 5.2.4.

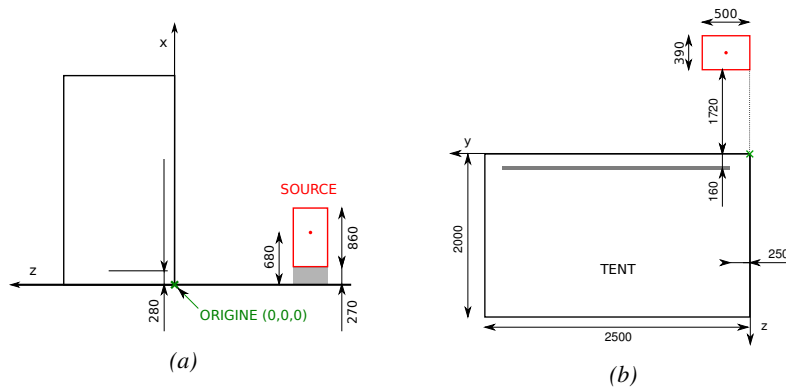


Figure 5.7: Description of the RPC setup. Dimensions are given in mm. A tent containing RPCs is placed at 1720 mm from the source container. The source is situated in the center of the container. RE-4-2-BARC-161 chamber is 160 mm inside the tent. This way, the distance between the source and the chambers plan is 2060 mm. Figure 5.7a provides a side view of the setup in the xz plane while Figure 5.7b shows a top view in the yz plane.

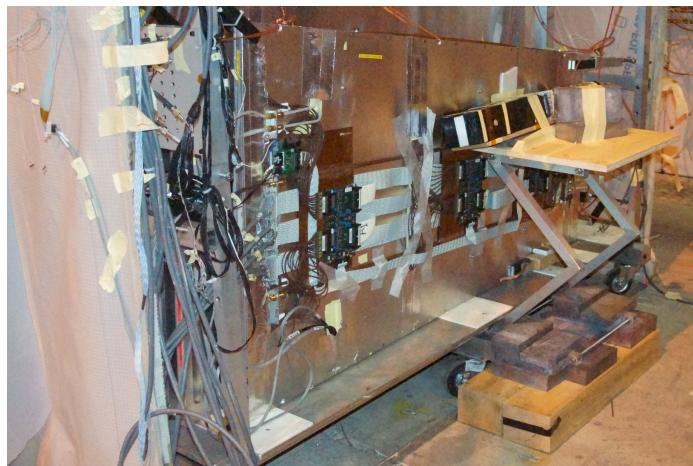


Figure 5.8: RE-4-2-BARC-161 chamber is inside the tent as described in Figure 5.7. In the top right, the two scintillators used as trigger can be seen. This trigger system has an inclination of 10° relative to horizontal and is placed above half-partition B2 of the RPCs. PMT electronics are shielded thanks to lead blocks placed in order to protect them without stopping photons from going through the scintillators and the chamber.

596 At the time of the tests, the beam not being operationnal anymore, a trigger
 597 composed of 2 plastic scintillators has been placed in front of the setup with an
 598 inclination of 10 deg with respect to the detector plane in order to look at cosmic
 599 muons. Using this particular trigger layout, shown on Figure 5.8, leads to a cosmic
 600 muon hit distribution into the chamber similar to the one in Figure 5.9. Measured
 601 without gamma irradiation, two peaks can be seen on the profil of partition B, cen-
 602 tered on strips 52 and 59. Section 5.2.3 will help us undertand that these two peaks
 603 are due respectively to forward and backward coming cosmic particles where for-
 604 ward coming particles are first detected by the scintillators and then the RPC while
 605 the backward coming muons are first detected in the RPC.

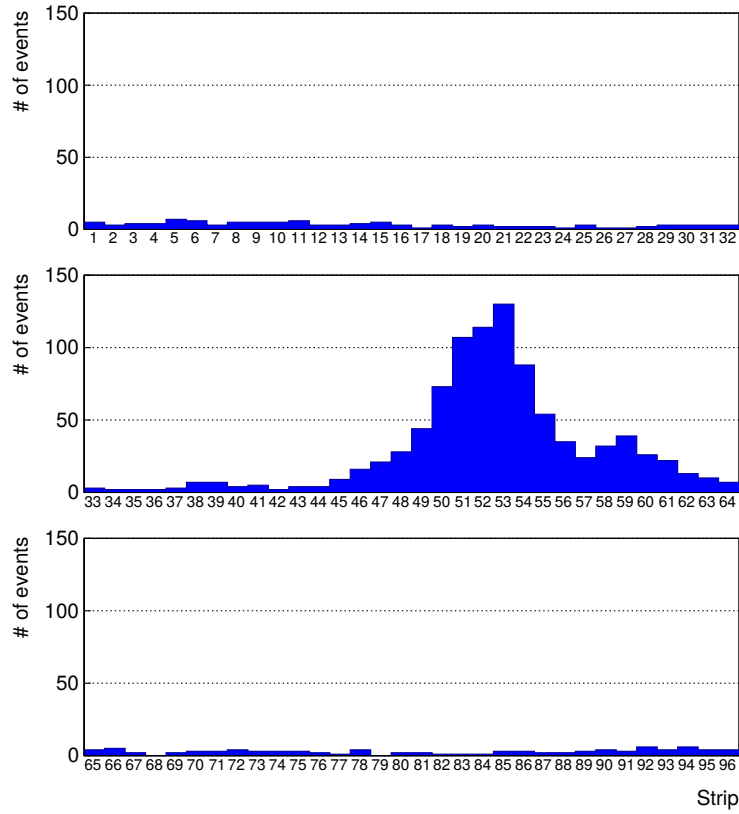


Figure 5.9: Hit distributions over all 3 partitions of RE-4-2-BARC-161 chamber is showed on these plots. Top, middle and bottom figures respectively correspond to partitions A, B, and C. These plots show that some events still occur in other half-partitions than B2, which corresponds to strips 49 to 64, in front of which the trigger is placed, contributing to the inefficiency of detection of cosmic muons. In the case of partitions A and C, the very low amount of data can be interpreted as noise. On the other hand, it is clear that a little portion of muons reach the half-partition B1, corresponding to strips 33 to 48.

5.2.2 Data Acquisition

5.2.3 Geometrical acceptance of the setup layout to cosmic muons

In order to profit from a constant gamma irradiation, the detectors inside of the GIF bunker need to be placed in a plane orthogonal to the beam line. The muon beam that used to be available was meant to test the performance of detectors under test. This beam not being active anymore, another solution to test detector performance had to be used. Thus, it has been decided to use cosmic muons detected through

a telescope composed of two scintillators. Lead blocks were used as shielding to protect the photomultipliers from gammas as can be seen from Figure 5.8.

An inclination has been given to the cosmic telescope to maximize the muon flux. A good compromise had to be found between good enough muon flux and narrow enough hit distribution to be sure to contain all the events into only one half partitions as required from the limited available readout hardware. Nevertheless, a consequence of the misplaced trigger, that can be seen as a loss of events in half-partition B1 in Figure 5.9, is an inefficiency. Nevertheless, the inefficiency of approximately 20 % highlighted in Figure 5.10 by comparing the performance of chamber BARC-161 in 904 and at GIF without irradiation seems too important to be explained only by the geometrical acceptance of the setup itself. Simulations have been conducted to show how the setup brings inefficiency.

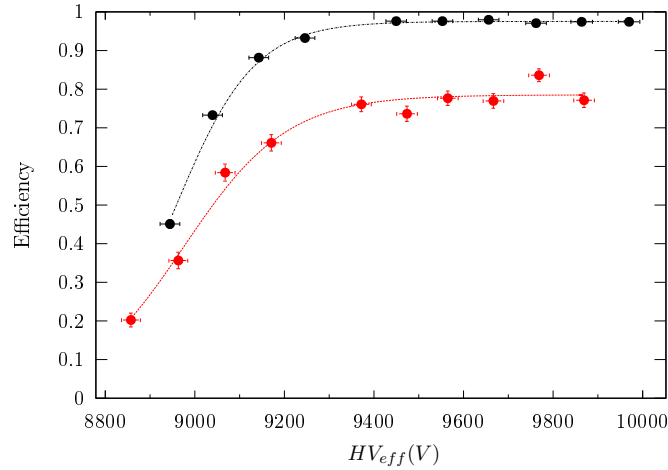


Figure 5.10: Results are derived from data taken on half-partition B2 only. On the 18th of June 2014, data has been taken on chamber RE-2-BARC-161 at building 904 (Preveessin Site) with cosmic muons providing us a reference efficiency plateau of $(97.54 \pm 0.15)\%$ represented by a black curve. A similar measurement has been done at GIF on the 21st of July with the same chamber giving a plateau of $(78.52 \pm 0.94)\%$ represented by a red curve.

5.2.3.1 Description of the simulation layout

The layout of GIF setup has been reproduced and incorporated into a Monte Carlo (MC) simulation to study the influence of the disposition of the telescope on the final distribution measured by the RPC. A 3D view of the simulated layout is given into Figure 5.11. Muons are generated randomly in a horizontal plane located at a height corresponding to the lowest point of the PMTs. This way, the needed size of the plane in order to simulate events happening at very big azimuthal angles (i.e.

632 $\theta \approx \pi$) can be kept relatively small. The muon flux is designed to follow the usual
 633 $\cos^2\theta$ distribution for cosmic particle. The goal of the simulation is to look at
 634 muons that pass through the muon telescope composed of the two scintillators and
 635 define their distribution onto the RPC plane. During the reconstruction, the RPC
 636 plane is then divided into its strips and each muon track is assigned to a strip.

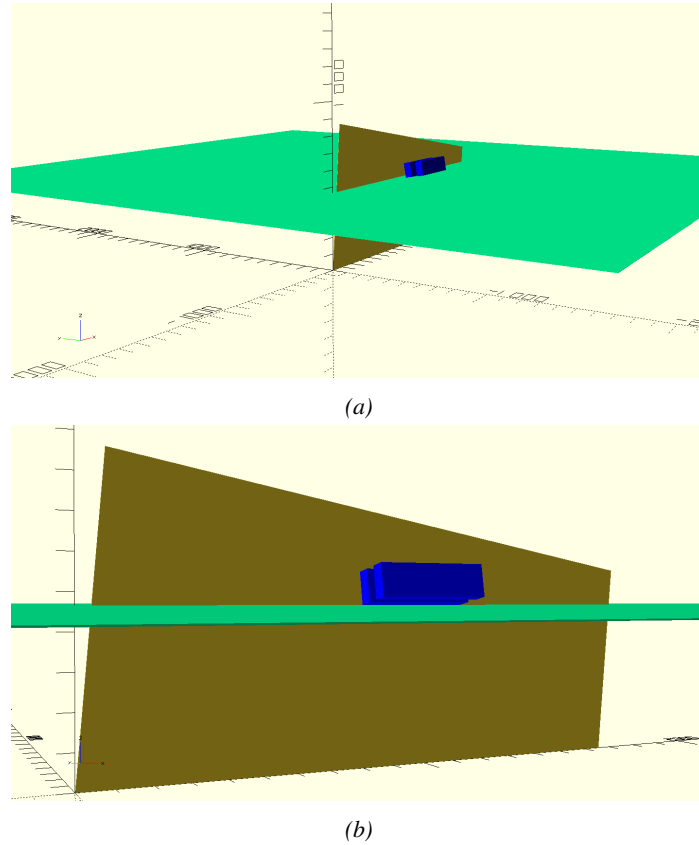


Figure 5.11: Representation of the layout used for the simulations of the test setup. The RPC is represented as a yellow trapezoid while the two scintillators as blue cuboids looking at the sky. A green plane corresponds to the muon generation plane within the simulation. Figure 5.7a shows a global view of the simulated setup. Figure 5.7b shows a zoomed view that allows to see the 2 scintillators as well as the full RPC plane.

637 In order to further refine the quality of the simulation and understand deeper
 638 the results the dependance of the distribution has been studied for a range of tele-
 639 scope inclinations. Moreover, the threshold applied on the PMT signals has been
 640 included into the simulation in the form of a cut. In the approximation of uni-
 641 form scintillators, it has been considered that the threshold can be understood as

the minimum distance particles need to travel through the scintillating material to give a strong enough signal. Particles that travel a distance smaller than the set "threshold" are thus not detected by the telescope and cannot trigger the data taking. Finally, the FEE threshold also has been considered in a similar way. The mean momentum of horizontal cosmic rays is higher than those of vertical ones but the stopping power of matter for momenta ranging from 1 GeV to 1 TeV stays comparable. It is then possible to assume that the mean number of primary e^-/ion pairs per unit length will stay similar and thus, depending on the applied discriminator threshold, muons with the shortest path through the gas volume will deposit less charge and induce a smaller signal on the pick-up strips that could eventually not be detected. These two thresholds also restrain the overall geometrical acceptance of the system.

5.2.3.2 Simulation procedure

The simulation software has been designed using C++ and the output data is saved into ROOT histograms. Simulations start for a threshold T_{scint} varying in a range from 0 to 45 mm in steps of 5 mm, where $T_{scint} = 0$ mm corresponds to the case where there isn't any threshold apply on the input signal while $T_{scint} = 45$ mm, which is the scintillator thickness, is the case where muons cannot arrive orthogonally onto the scintillator surface. For a given T_{scint} , a set of RPC thresholds are considered. The RPC threshold, T_{RPC} varies from 2 mm, the thickness of the gas volume, to 3 mm in steps of 0.25 mm. For each $(T_{scint}; T_{RPC})$ pair, $N_\mu = 10^8$ muons are randomly generated inside the muon plane described in the previous paragraph with an azimuthal angle θ chosen to follow a $\cos^2\theta$ distribution.

Planes are associated to each surface of the scintillators. Knowing muon position into the muon plane and its direction allows us, by assuming that muons travel in a straight line, to compute the intersection of the muon track with these planes. Applying conditions to the limits of the surfaces of the scintillator faces then gives us an answer to whether or not the muon passed through the scintillators. In the case the muon has indeed passed through the telescope, the path through each scintillator is computed and muons whose path was shorter than T_{scint} are rejected and are thus considered as having not interacted with the setup.

On the contrary, if the muon is labeled as good, its position within the RPC plane is computed and the corresponding strip, determined by geometrical tests in the case the distance through the gas volume was enough not to be rejected because of T_{RPC} , gets a hit and several histograms are filled in order to keep track of the generation point on the muon plane, the intersection points of the reconstructed muons within the telescope, or on the RPC plane, the path traveled through each individual scintillator or the gas volume, as well as other histograms. Moreover, muons fill different histograms whether they are forward or backward coming muons. They are discriminated according to their direction components.

When a muon is generated, an (x, y, z) position is assigned into the muon plane as well as a $(\theta; \phi)$ pair that gives us the direction it's coming from. This way, muons satisfying the condition $0 \leq \phi < \pi$ are designated as backward coming muons while muons satisfying $\pi \leq \phi < 2\pi$ as forward coming muons.

This simulation is then repeated for different telescope inclinations ranging in between 4 and 20° and varying in steps of 2° . Due to this inclination and to the vertical position of the detector under test, the muon distribution reconstructed in the detector plane is asymmetrical. The choice as been made to chose a skew distribution formula to fit the data built as the multiplication of gaussian and sigmoidal curves together. A typical gaussian formula is given as 5.1 and has three free parameters as A_g , its amplitude, \bar{x} , its mean value and σ , its root mean square. Sigmoidal curves as given by formula 5.2 are functions converging to 0 and A_s as x diverges. The inflexion point is given as x_i and λ is proportional to the slope at $x = x_i$. In the limit where $\lambda \rightarrow \infty$, the sigmoid becomes a step function.

$$g(x) = A_g e^{\frac{-(x-\bar{x})^2}{2\sigma^2}} \quad (5.1)$$

$$s(x) = \frac{A_s}{1 + e^{-\lambda(x-x_i)}} \quad (5.2)$$

Finally, a possible representation of a skew distribution is given by formula 5.3 and is the product of 5.1 and 5.2. Naturally, here $A_{sk} = A_g \times A_s$ and represents the theoretical maximum in the limit where the skew tends to a gaussian function.

$$sk(x) = g(x) \times s(x) = A_{sk} \frac{e^{\frac{-(x-\bar{x})^2}{2\sigma^2}}}{1 + e^{-\lambda(x-x_i)}} \quad (5.3)$$

5.2.3.3 Results

Influence of T_{scint} on the muon distribution

Influence of T_{RPC} on the muon distribution

Influence of the telescope inclination on the muon distribution

Comparison to data taken at GIF without irradiation

5.2.4 Photon flux at GIF

5.2.4.1 Expectations from simulations

In order to understand and evaluate the γ flux in the GIF area, simulations had been conducted in 1999 and published by S. Agosteo et al [6]. Table 5.1 presented in this article gives us the γ flux for different distances D to the source. This simulation was done using GEANT and a Monte Carlo N-Particle (MCNP) transport code, and the flux F is given in number of γ per unit area and unit time along with the estimated error from these packages expressed in %.

Nominal ABS	Photon flux F [$s^{-1}cm^{-2}$]			
	at $D = 50$ cm	at $D = 155$ cm	at $D = 300$ cm	at $D = 400$ cm
1	$0.12 \cdot 10^8 \pm 0.2\%$	$0.14 \cdot 10^7 \pm 0.5\%$	$0.45 \cdot 10^6 \pm 0.5\%$	$0.28 \cdot 10^6 \pm 0.5\%$
2	$0.68 \cdot 10^7 \pm 0.3\%$	$0.80 \cdot 10^6 \pm 0.8\%$	$0.25 \cdot 10^6 \pm 0.8\%$	$0.16 \cdot 10^6 \pm 0.6\%$
5	$0.31 \cdot 10^7 \pm 0.4\%$	$0.36 \cdot 10^6 \pm 1.2\%$	$0.11 \cdot 10^6 \pm 1.2\%$	$0.70 \cdot 10^5 \pm 0.9\%$

Table 5.1: Total photon flux ($E\gamma \leq 662$ keV) with statistical error predicted considering a ^{137}Cs activity of 740 GBq at different values of the distance D to the source along the x -axis of irradiation field [6].

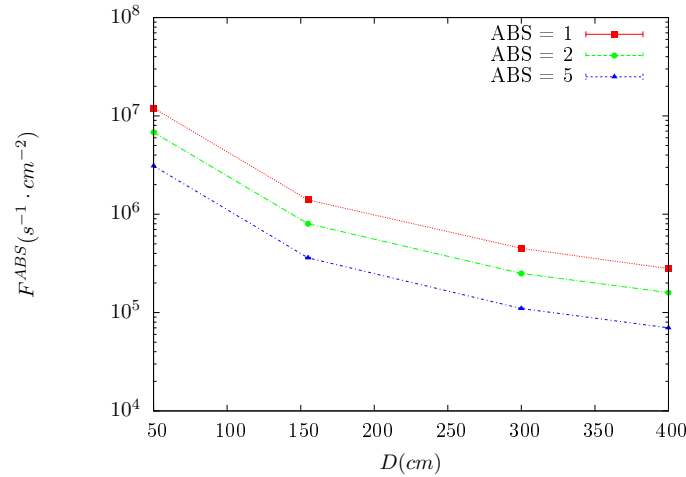


Figure 5.12: γ flux $F(D)$ is plot using values from table 5.1. As expected, the plot shows similar attenuation behaviours with increasing distance for each absorption factors.

The simulation doesn't directly provides us with an estimated flux at the level of our RPC. First of all, it is needed to extract the value of the flux from the available data contained in the original paper and then to estimate the flux in 2014 at the time the experimentation took place. Figure 5.12 that contains the data from

Table 5.1. In the case of a pointlike source emitting isotrope and homogeneous gamma radiations, the gamma flux F at a distance D to the source with respect to a reference point situated at D_0 where a known flux F_0 is measured will be expressed like in Equation 5.4, assuming that the flux decreases as $1/D^2$, where c is a fitting factor.

$$F^{ABS} = F_0^{ABS} \times \left(\frac{cD_0}{D} \right)^2 \quad (5.4)$$

By rewriting Equation 5.4, it comes that :

$$c = \frac{D}{D_0} \sqrt{\frac{F^{ABS}}{F_0^{ABS}}} \quad (5.5)$$

$$\Delta c = \frac{c}{2} \left(\frac{\Delta F^{ABS}}{F^{ABS}} + \frac{\Delta F_0^{ABS}}{F_0^{ABS}} \right) \quad (5.6)$$

Finally, using Equation 5.5 and the data in Table 5.1 with $D_0 = 50$ cm as reference point, we can build Table 5.2. It is interesting to note that c for each value of D doesn't depend on the absorption factor.

Nominal ABS	Correction factor c		
	at $D = 155$ cm	at $D = 300$ cm	at $D = 400$ cm
1	$1.059 \pm 0.70\%$	$1.162 \pm 0.70\%$	$1.222 \pm 0.70\%$
2	$1.063 \pm 1.10\%$	$1.150 \pm 1.10\%$	$1.227 \pm 0.90\%$
5	$1.056 \pm 1.60\%$	$1.130 \pm 1.60\%$	$1.202 \pm 1.30\%$

Table 5.2: Correction factor c is computed thanks to formulae 5.5 taking as reference $D_0 = 50$ cm and the associated flux F_0^{ABS} for each absorption factor available in table 5.1.

For the range of D/D_0 values available, it is possible to use a simple linear fit to get the evolution of c . The linear fit will then use only 2 free parameters, a and b , as written in Equation 5.7. This gives us the results showed in Figure 5.13. Figure 5.13b confirms that using only a linear fit to extract c is enough as the evolution of the rate that can be obtained superimposes well on the simulation points.

$$c \left(\frac{D}{D_0} \right) = a \frac{D}{D_0} + b \quad (5.7)$$

$$F^{ABS} = F_0^{ABS} \left(a + \frac{bD_0}{D} \right)^2 \quad (5.8)$$

$$\Delta F^{ABS} = F^{ABS} \left[\frac{\Delta F_0^{ABS}}{F_0^{ABS}} + 2 \frac{\Delta a + \Delta b \frac{D_0}{D}}{a + \frac{bD_0}{D}} \right] \quad (5.9)$$

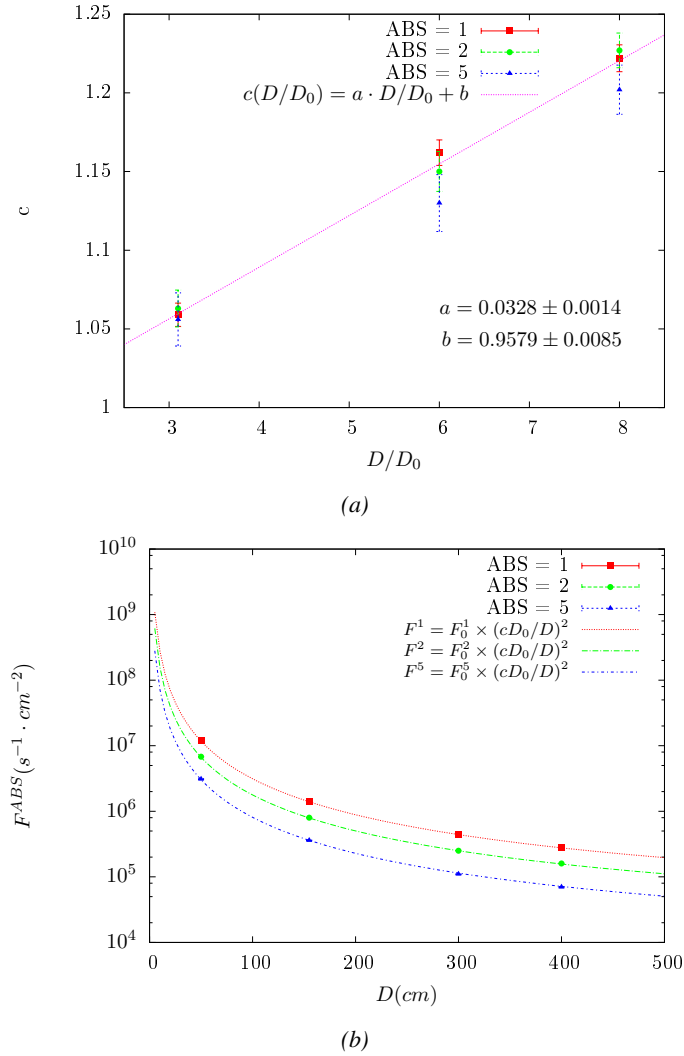


Figure 5.13: Figure 5.13a shows the linear approximation fit done via formulae 5.7 on data from table 5.2. Figure 5.13b shows a comparison of this model with the simulated flux using a and b given in figure 5.13a in formulae 5.4 and the reference value $D_0 = 50cm$ and the associated flux for each absorption factor F_0^{ABS} from table 5.1

731 In the case of the 2014 GIF tests, the RPC plane is located at a distance
 732 $D = 206 cm$ to the source. Moreover, to estimate the strength of the flux in 2014,
 733 it is necessary to consider the nuclear decay through time associated to the Cesium
 734 source whose half-life is well known ($t_{1/2} = (30.05 \pm 0.08) y$). The very first
 735 source activity measurement has been done on the 5th of March 1997 while the

GIF tests were done in between the 20th and the 31st of August 2014, i.e. at a time $t = (17.47 \pm 0.02)$ y resulting in an attenuation of the activity from 740 GBq in 1997 to 494 GBq in 2014. All the needed information to extrapolate the flux through our detector in 2014 has now been assembled, leading to the Table 5.3. It is interesting to note that for a common RPC sensitivity to γ of $2 \cdot 10^{-3}$, the order of magnitude of the estimated hit rate per unit area is of the order of the kHz for the fully opened source. Moreover, taking profit of the two working absorbers, it will be possible to scan background rates at 0 Hz, ~ 300 Hz as well as ~ 600 Hz. Without source, a good estimate of the intrinsic performance will be available. Then at 300 Hz, the goal will be to show that the detectors fulfill the performance certification of CMS RPCs. Then a first idea of the performance of the detectors at higher background will be provided with absorption factors 2 (~ 600 Hz) and 1 (no absorption). *[Here I will also put a reference to the plot showing the estimated background rate at the level of RE3/1 in the case of HL-LHC but this one being in another chapter, I will do it later.]*

Nominal ABS	Photon flux F [$\text{s}^{-1}\text{cm}^{-2}$]			Hit rate/unit area [Hz cm^{-2}] at $D^{2014} = 206$ cm
	at $D_0^{1997} = 50$ cm	at $D^{1997} = 206$ cm	at $D^{2014} = 206$ cm	
1	$0.12 \cdot 10^8 \pm 0.2\%$	$0.84 \cdot 10^6 \pm 0.3\%$	$0.56 \cdot 10^6 \pm 0.3\%$	1129 ± 32
2	$0.68 \cdot 10^7 \pm 0.3\%$	$0.48 \cdot 10^6 \pm 0.3\%$	$0.32 \cdot 10^6 \pm 0.3\%$	640 ± 19
5	$0.31 \cdot 10^7 \pm 0.4\%$	$0.22 \cdot 10^6 \pm 0.3\%$	$0.15 \cdot 10^6 \pm 0.3\%$	292 ± 9

Table 5.3: The data at D_0 in 1997 is taken from [6]. In a second step, using Equations 5.8 and 5.9, the flux at D can be estimated in 1997. Then, taking into account the attenuation of the source activity, the flux at D can be estimated at the time of the tests in GIF in 2014. Finally, assuming a sensitivity of the RPC to γ $s = 2 \cdot 10^{-3}$, an estimation of the hit rate per unit area is obtained.

751 **5.2.4.2 Dose measurements**

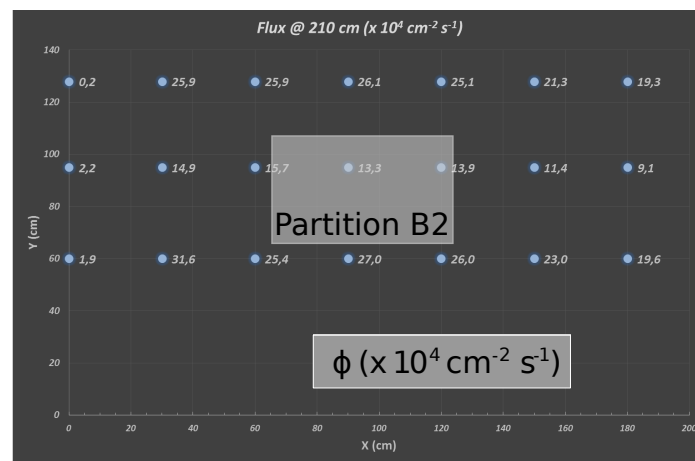


Figure 5.14: Dose measurements has been done in a plane corresponding to the tents front side. This plan is 1900 mm away from the source. As explained in the first chapter, a lens-shaped lead filter provides a uniform photon flux in the vertical plan orthogonal to the beam direction. If the second line of measured fluxes is not taken into account because of lower values due to experimental equipments in the way between the source and the tent, the uniformity of the flux is well showed by the results.

752 **5.2.5 Results and discussions**

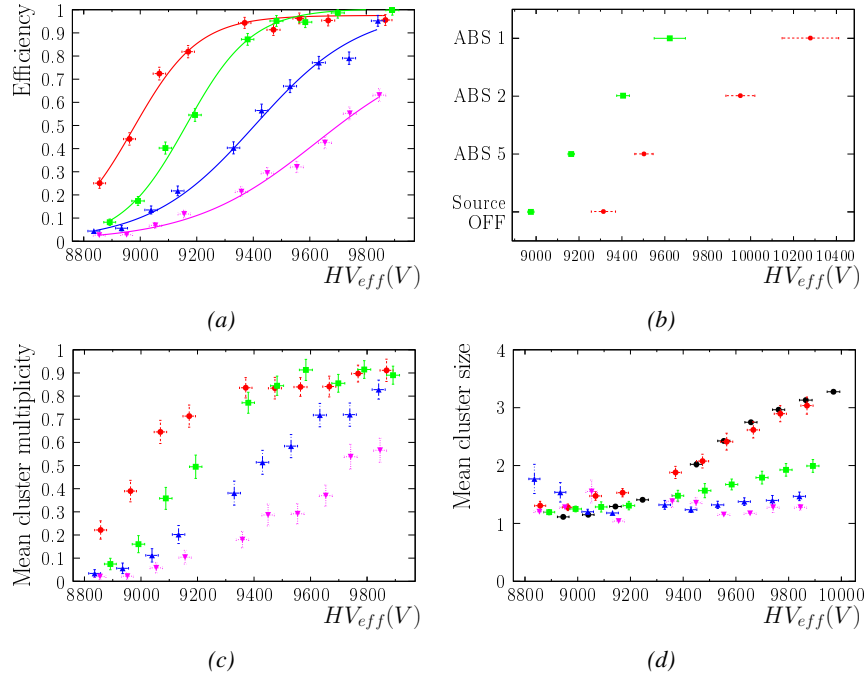


Figure 5.15

5.3 Longevity tests at GIF++

Longevity studies imply a monitoring of the performance of the detectors probed using a high intensity muon beam in a irradiated environment by periodically measuring their rate capability, the dark current running through them and the bulk resistivity of the Bakelite composing their electrodes. GIF++, with its very intense ^{137}Cs source, provides the perfect environment to perform such kind of tests. Assuming a maximum acceleration factor of 3, it is expected to accumulate the equivalent charge in 1.7 years.

As the maximum background is found in the endcap, the choice naturally was made to focus the GIF++ longevity studies on endcap chambers. Most of the RPC system was installed in 2007. Nevertheless, the large chambers in the fourth endcap (RE4/2 and RE4/3) have been installed during LS1 in 2014. The Bakelite of these two different productions having different properties, four spare chambers of the present system were selected, two RE2,3/2 spares and two RE4/2 spares. Having two chambers of each type allows to always keep one of them non irradiated as reference, the performance evolution of the irradiated chamber being then compared through time to the performance of the non irradiated one.

The performance of the detectors under different level of irradiation is measured periodically during dedicated test beam periods using the H4 muon beam. In between these test beam periods, the two RE2,3/2 and RE4/2 chambers selected for this study are irradiated by the ^{137}Cs source in order to accumulate charge and the gamma background is monitored, as well as the currents. The two remaining chambers are kept non-irradiated as reference detectors. Due to the limited gas flow in GIF++, the RE4 chamber remained non-irradiated until end of November 2016 where a new mass flow controller has been installed allowing for bigger volumes of gas to flow in the system.

Figures 5.16 and 5.17 give us for different test beam periods, and thus for increasing integrated charge through time, a comparison of the maximum efficiency, obtained using a sigmoid-like function, and of the working point of both irradiated and non irradiated chambers [9]. No aging is yet to see from this data, the shifts in γ rate per unit area in between irradiated and non irradiated detectors and RE2 and RE4 types being easily explained by a difference of sensitivity due to the various Bakelite resistivities of the HPL electrodes used for the electrode production.

Collecting performance data at each test beam period allows us to extrapolate the maximum efficiency for a background hit rate of 300 Hz/cm^2 corresponding to the expected HL-LHC conditions. Aging effects could emerge from a loss of efficiency with increasing integrated charge over time, thus Figure 5.18 helps us understand such degradation of the performance of irradiated detectors in comparison with non irradiated ones. The final answer for an eventual loss of efficiency is given in Figure 5.19 by comparing for both irradiated and non irradiated detectors

the efficiency sigmoids before and after the longevity study. Moreover, to complete the performance information, the Bakelite resistivity is regularly measured thanks to Ag scans (Figure 5.20) and the noise rate is monitored weekly during irradiation periods (Figure 5.21). At the end of 2016, no signs of aging were observed and further investigation is needed to get closer to the final integrated charge requirements proposed for the longevity study of the present CMS RPC sub-system.

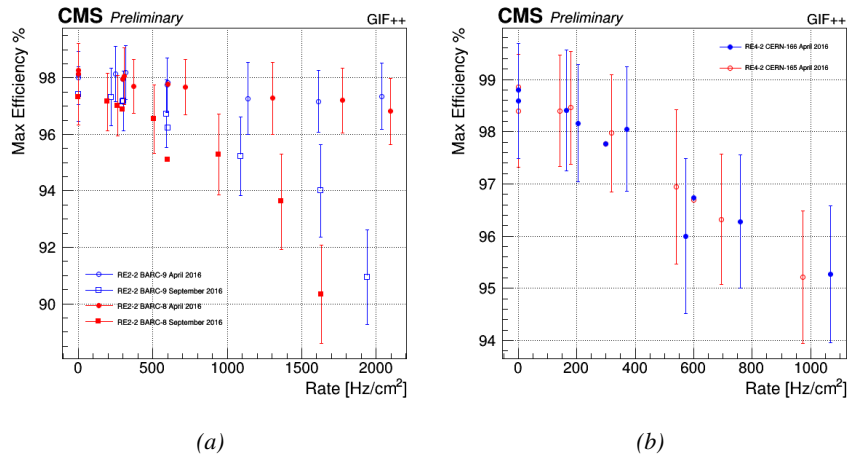


Figure 5.16: Evolution of the maximum efficiency for RE2 (5.16a) and RE4 (5.16b) chambers with increasing extrapolated γ rate per unit area at working point. Both irradiated (blue) and non irradiated (red) chambers are shown.

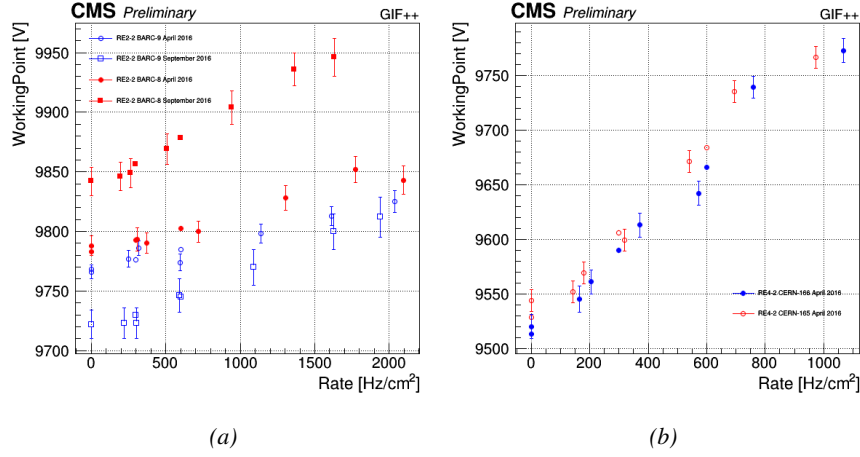


Figure 5.17: Evolution of the working point for RE2 (5.17a) and RE4 (5.17b) with increasing extrapolated γ rate per unit area at working point. Both irradiated (blue) and non irradiated (red) chambers are shown.

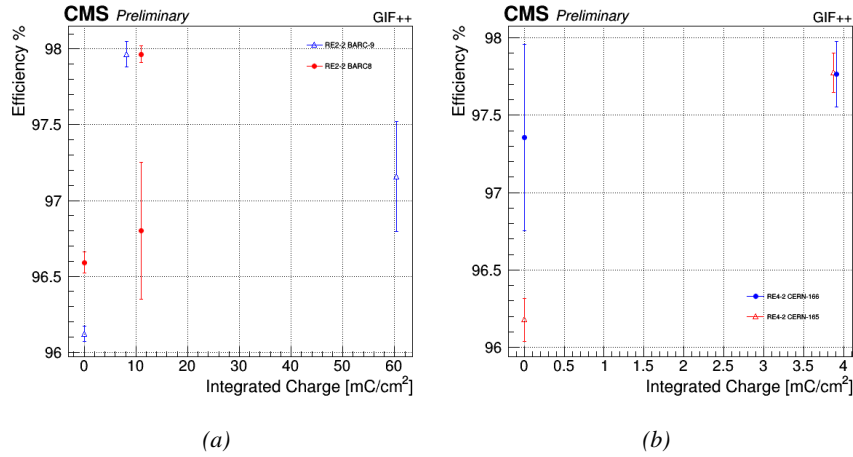


Figure 5.18: Evolution of the maximum efficiency at HL-LHC conditions, i.e. a background hit rate per unit area of 300 Hz/cm², with increasing integrated charge for RE2 (5.18a) and RE4 (5.18b) detectors. Both irradiated (blue) and non irradiated (red) chambers are shown. The integrated charge for non irradiated detectors is recorded during test beam periods and stays small with respect to the charge accumulated in irradiated chambers.

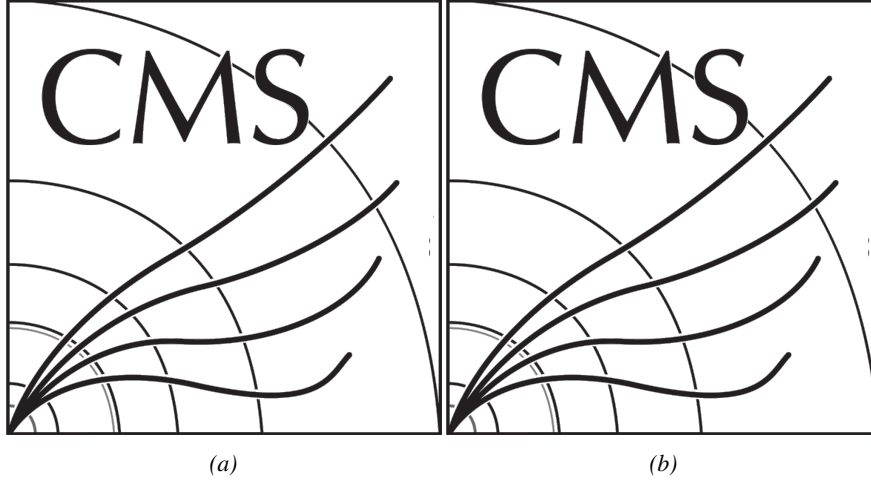


Figure 5.19: Comparison of the efficiency sigmoid before (triangles) and after (circles) irradiation for RE2 (5.19a) and RE4 (5.19b) detectors. Both irradiated (blue) and non irradiated (red) chambers are shown.

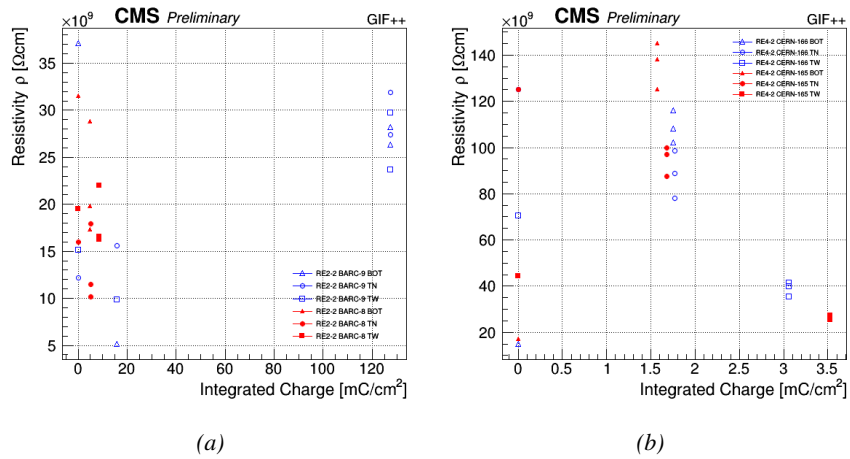


Figure 5.20: Evolution of the Bakelite resistivity for RE2 (5.20a) and RE4 (5.20b) detectors. Both irradiated (blue) and non irradiated (red) chambers are shown.

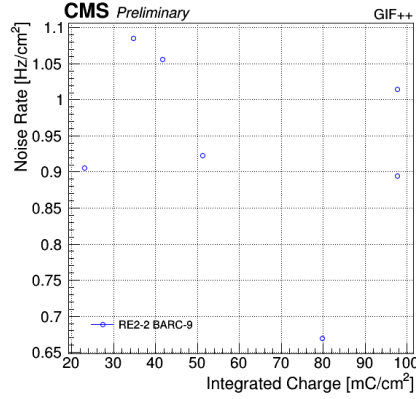


Figure 5.21: Evolution of the noise rate per unit area for the irradiated chamber RE2-2-BARC-9 only.

5.3.1 Description of the Data Acquisition

For the longevity studies, four spare chambers of the present system are used. Two spare RPCs of the RE2,3 stations as well as two spare RPCs from the new RE4 stations have been mounted in a Trolley. Six RE4 gaps are also placed in the trolley. The trolley is placed inside the GIF++ in the upstream region of the bunker, taking the cesium source as a reference. The trolley is oriented for the detection surface of the chambers to be orthogonal to the beam line. The system can be moved along the orthogonal plane in order to have the beam in all η -partitions. For the aging the trolley is moved outside the beam line and is placed in a distance of 5.2 m to the source, which irradiates the bunker using an attenuation filter of 2.2 which corresponds to a fluence of 10^7 gamma/cm².

During GIF++ operation, the data collected can be divided into different categories as several parameters are monitored in addition to the usual RPC performance data. On one hand, to know the performance of a chamber, it is need to measure its efficiency and to know the background conditions in which it is operated. To do this, the hit signals from the chamber are recorded and stored in a ROOT file via a Data Acquisition (DAQ) software. On the other hand, it is also very important to monitor parameters such as environmental pressure and temperature, gas temperature and humidity, RPC HV, LV, and currents, or even source and beam status. This is done through the GIF++ web Detector Control Software (DCS) that stores this information in a database.

Two different types of tests are conducted on RPCs via the DAQ. Indeed, the performance of the detectors is measured periodically during dedicated test beam periods using the H4 muon beam. In between these test beam periods, when the beam is not available, the chambers are irradiated by the ¹³⁷Cs in order to accu-

825 mulate deposited charge and the gamma background is measured.

826 RPCs under test are connected through LVDS cables to V1190A Time-to-
827 Digital Converter (TDC) modules manufactured by CAEN. These modules, lo-
828 cated in the rack area outside of the bunker, get the logic signals sent by the cham-
829 bers and save them into their buffers. Due to the limited size of the buffers, the
830 collected data is regularly erased and replaced. A trigger signal is needed for the
831 TDC modules to send the useful data to the DAQ computer via a V1718 CAEN
832 USB communication module.

833 In the case of performance test, the trigger signal used for data acquisition is
834 generated by the coincidence of three scintillators. A first one is placed upstream
835 outside of the bunker, a second one is placed downstream outside of the bunker,
836 while a third one is placed in front of the trolley, close by the chambers. Every time
837 a trigger is sent to the TDCs, i.e. every time a muon is detected, knowing the time
838 delay in between the trigger and the RPC signals, signals located in the right time
839 window are extracted from the buffers and saved for later analysis. Signals are
840 taken in a time window of 400 ns centered on the muon peak (here we could show
841 a time spectrum). On the other hand, in the case of background rate measurement,
842 the trigger signal needs to be "random" not to measure muons but to look at gamma
843 background. A trigger pulse is continuously generated at a rate of 300 Hz using a
844 dual timer. To integrate an as great as possible time, all signals contained within
845 a time window of 10us prior to the random trigger signal are extracted from the
846 buffers and saved for further analysis (here another time spectrum to illustrate
847 could be useful, maybe even place both spectrum together as a single Figure).

848 The signals sent to the TDCs correspond to hit collections in the RPCs. When a
849 particle hits a RPC, it induce a signal in the pickup strips of the RPC readout. If this
850 signal is higher than the detection threshold, a LVDS signal is sent to the TDCs.
851 The data is then organised into 4 branches keeping track of the event number, the
852 hit multiplicity for the whole setup, and the time and channel profile of the hits in
853 the TDCs.

854 **5.3.2 RPC current, environmental and operation parameter mon-** 855 **itoring**

856 In order to take into account the variation of pressure and temperature between
857 different data taking periods the applied voltage is corrected following the rela-
858 tionship :

$$HV_{eff} = HV_{app} \times \left(0.2 + 0.8 \cdot \frac{P_0}{P} \times \frac{T}{T_0} \right) \quad (5.10)$$

859 where T_0 (=293 K) and P_0 (=990 mbar) are the reference values.

860 **5.3.3 Measurement procedure**

861 Insert a short description of the online tools (DAQ, DCS, DQM).

862 Insert a short description of the offline tools : tracking and efficiency algorithm.

863 Identify long term aging effects we are monitoring the rates per strip.

864 **5.3.4 Longevity studies results**

6

865

866

Investigation on high rate RPCs

867 **6.1 Rate limitations and ageing of RPCs**

868 **6.1.1 Low resistivity electrodes**

869 **6.1.2 Low noise front-end electronics**

870 **6.2 Construction of prototypes**

871 **6.3 Results and discussions**

7

872

873

Conclusions and outlooks

874 **7.1 Conclusions**

875 **7.2 Outlooks**

References

- 877 [1] CERN. Geneva. LHC Experiments Committee. *The CMS muon project :
878 Technical Design Report*. Tech. rep. CERN-LHCC-97-032. CMS Collabo-
879 ration, 1997.
- 880 [2] CERN. Geneva. LHC Experiments Committee. *Technical Proposal for the
881 Phase-II Upgrade of the CMS Detector*. Tech. rep. CERN-LHCC-2015-010.
882 CMS Collaboration, 2015.
- 883 [3] CERN. Geneva. LHC Experiments Committee. *CMS, the Compact Muon
884 Solenoid : technical proposal*. Tech. rep. CERN-LHCC-94-38. CMS Col-
885 laboration, 1994.
- 886 [4] M. Abbrescia et al. “Study of long-term performance of CMS RPC under
887 irradiation at the CERN GIF”. In: *NIMA* 533 (2004), pp. 102–106.
- 888 [5] H.C. Kim et al. “Quantitative aging study with intense irradiation tests for
889 the CMS forward RPCs”. In: *NIMA* 602 (2009), pp. 771–774.
- 890 [6] S. Agosteo et al. “A facility for the test of large-area muon chambers at high
891 rates”. In: *NIMA* 452 (2000), pp. 94–104.
- 892 [7] PoS, ed. *CERN GIF ++ : A new irradiation facility to test large-area par-
893 ticle detectors for the high-luminosity LHC program*. Vol. TIPP2014. 2014,
894 pp. 102–109.
- 895 [8] CAEN. *Mod. V1190-VX1190 A/B, 128/64 Ch Multihit TDC*. 13th ed. 2012.
- 896 [9] M. Abbrescia et al. “Cosmic ray tests of double-gap resistive plate chambers
897 for the CMS experiment”. In: *NIMA* 550 (2005), pp. 116–126.
- 898 [10] A. Fagot. *GIF++ DAQ v4.0*. 2017. URL: [https://github.com/
899 afagot/GIF_DAQ](https://github.com/afagot/GIF_DAQ).



900

901

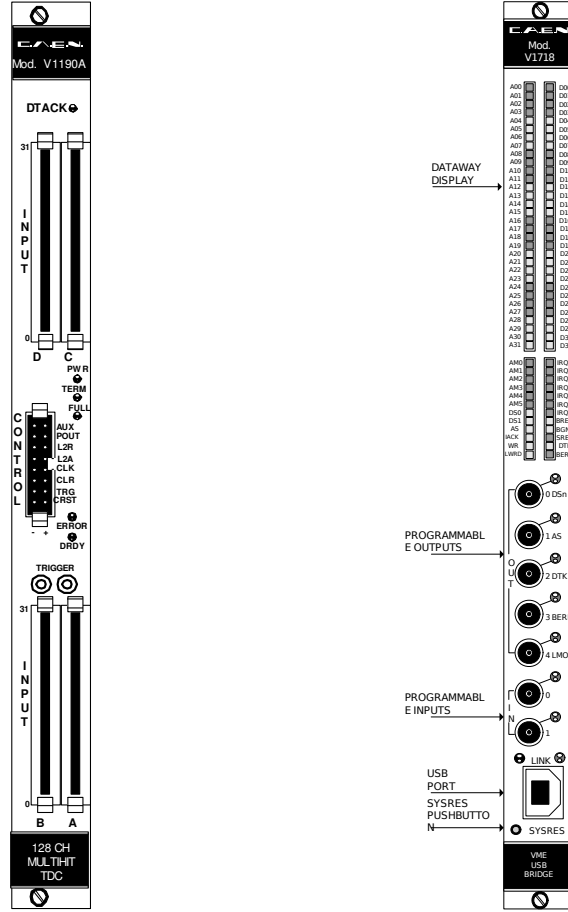
902

A data acquisition software for CAEN VME TDCs

903 Certifying detectors in the perspective of HL-LHC required to develop tools for
904 the GIF++ experiment. Among them was the Data Acquisition (DAQ) software
905 that allows to make the communications in between the computer and the TDC
906 modules in order to retrieve the RPC data [10]. In this appendix, details about the
907 software, as of how the software was written, how it functions and how it can be
908 exported to another similar setup.

909 **A.1 Description of the setup**

910 The CMS RPC setup at GIF++ counts 5 V1190A Time-to-Digital Converter (TDC)
911 manufactured by CAEN [8]. The communication between the computer and the
912 TDCs to transfer data is done via a V1718 VME master module also manufactured
913 by CAEN and operated from a USB port [V1718MUT]. These VME modules are
914 hosted into a 6U VME 6021 powered crate manufactured by W-Ie-Ne-R than can
915 accomodate up to 21 VME bus cards [6U6000MUT]. These 3 components of the
916 DAQ setup are shown in Figure A.1.



(a)

(b)



(c)

Figure A.1: (A.1a) View of the front panel of a VI190A TDC module [8]. (A.1b) View of the front panel of a VI718 Bridge module [V1718MUT]. (A.1c) View of the front panel of a 6U 6021 VME crate [6U6000MUT].

A.2 Data read-out

To efficiently perform a data readout algorithm, objects to handle the VME modules (TDCs and VME bridge) have been created along with objects to store data and read the configuration file that comes as an input of the DAQ software.

It is useful to remind that the DAQ software in GIF++ is not a standalone software but it is called by a **webDCS!** (webDCS) application, that is the core of interactions with GIF++ setup, when data needs to be taken. But it is straight forward to turn it into a standalone program that could be adapted to any VME setup using V1190A and V1718 modules.

A.2.1 V1190A TDCs

The DAQ used at GIF takes profit of the *Trigger Matching Mode* offered by V1190A modules. A trigger matching is performed in between a trigger time tag and the channel time measurements. Control over this data acquisition mode, explained through Figure A.2, is offered through 4 programmable parameters:

- **match window:** the match between a trigger and a hit is done within a programmable time window. This is set via the method

```
v1190a::SetTrigWindowWidth(Uint windowWidth, int ntdcs)
```

- **window offset:** temporal distance between the trigger tag and the start of the trigger matching window. This is set via the method

```
v1190a::SetTrigWindowWidth(Uint windowWidth, int ntdcs)
```

- **extra search margin:** an extended time window is used to ensure that all matching hits are found. This is set via the method

```
v1190a::SetTrigSearchMargin(Uint searchMargin, int ntdcs)
```

- **reject margin:** older hits are automatically rejected to preven buffer overflows and to speed up the search time. This is set via the method

```
v1190a::SetTrigRejectionMargin(Uint rejectMargin, int ntdcs)
```

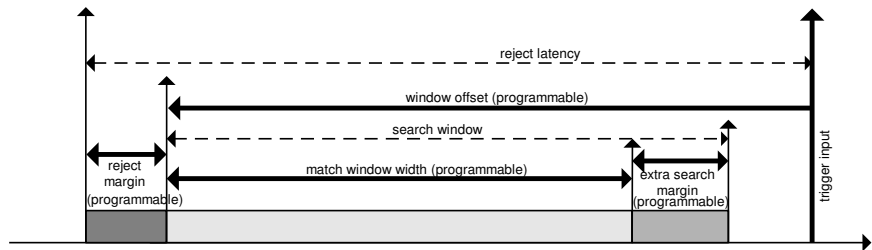


Figure A.2: Module V1190A Trigger Matching Mode timing diagram [8].

Each of these 4 parameters are given in number of clocks, 1 clock being 25 ns long. It is easy to understand at this level that there are 3 possible functioning settings:

- **1:** the match window is entirely contained after the trigger signal,
- **2:** the match window overlaps the trigger signal, or
- **3:** the match window is entirely contained before the trigger signal as displayed on Figure A.2.

In both the first and second cases, the sum of the window width of the offset can be set at maximum to be 40 clocks, which corresponds to 1 μ s. Of course, the offset can be negative thus allowing for a longer match window, its end being at maximum 1 μ s after the trigger signal. In the third case, the maximum negative offset allowed is of 2048 clocks (12 bit) corresponding to 51.2 μ s, the match window being strictly smaller than the offset. In the case of GIF++, the choice has been made to use this last setting by delaying the trigger signal. During the studies performed in GIF++, both the efficiency of the RPCs, using a muon beam, and the noise or gamma background rate are monitored. The extra search and reject margins are left unused.

To probe the efficiency of RPC detectors, a signal provided by the coincidence of scintillators when a bunch of muons passes through the area is used to trigger the data acquisition. For this measurement, it is useful to reduce the match window width only to contain the muon information. Indeed, the delay in between a trigger signal and the detection of the corresponding muon in the RPC being very constant (typically a few tens of ns due to jitter and cable length), the muon signals are very localised in time. Thus the settings were chosen to have a window width of 24 clocks (600 ns) and a negative offset of 29 clocks.

On the otherhand, monitoring the rates doesn't require for the DAQ to look at a specific time window. It is important to integrate as much time as possible to have a robust measurement of the rate as the number of hits per time unit. The triggering signal is provided by a pulse generator at a frequency of 300 Hz to ensure that the data taking occurs in a random way to probe only the irradiation spectrum on the detectors. The match window is set to 400 clocks (10 μ s) and the negative offset to 401 clocks as it needs to exceed the value of the match window.

The v1190a object, defined in the DAQ software as followed, offer the possibility to concatenate all TDCs in the setup into a single object containing a list of hardware addresses (addresses to access the TDC buffer through the VME crate) and each constructor and method acts on the list of TDCs.

```

class v1190a
{
private :
    long          Handle;
    vector<Data32> Address;
    CVDataWidth   DataWidth;
    CVAddressModifier AddressModifier;

public:

    v1190a(long handle, IniFile *infile, int ntdcs);
    ~v1190a();
    Data16 write_op_reg(Data32 address, int code, string error);
    Data16 read_op_reg(Data32 address, string error);
    void Reset(int ntdcs);
    void Clear(int ntdcs);
    void TestWR(Data16 value, int ntdcs);
    void CheckTDCStatus(int ntdcs);
    void CheckCommunication(int ntdcs);
    void SetTDCTestMode(Data16 mode, int ntdcs);
    void SetTrigMatching(int ntdcs);
981 void SetTrigTimeSubtraction(Data16 mode, int ntdcs);
    void SetTrigWindowWidth(UINT windowWidth, int ntdcs);
    void SetTrigWindowOffset(UINT windowOffset, int ntdcs);
    void SetTrigSearchMargin(UINT searchMargin, int ntdcs);
    void SetTrigRejectionMargin(UINT rejectMargin, int ntdcs);
    void GetTrigConfiguration(int ntdcs);
    void SetTrigConfiguration(IniFile *infile, int ntdcs);
    void SetTDCDetectionMode(Data16 mode, int ntdcs);
    void SetTDCResolution(Data16 lsb, int ntdcs);
    void SetTDCDeadTime(Data16 time, int ntdcs);
    void SetTDCHeadTrailer(Data16 mode, int ntdcs);
    void SetTDCEventSize(Data16 size, int ntdcs);
    void SwitchChannels(IniFile *infile, int ntdcs);
    void SetIRQ(Data32 level, Data32 count, int ntdcs);
    void SetBlockTransferMode(Data16 mode, int ntdcs);
    void Set(IniFile *infile, int ntdcs);
    void CheckStatus(CVErrorCodes status) const;
    int ReadBlockD32(UINT tdc, const Data16 address,
                    Data32 *data, const UINT words, bool ignore_berr);
    UINT Read(RAWData *DataList, int ntdcs);
};

```

982 A.2.2 V1718 USB Bridge

983 As previously described in Section 4.4.3, CMS RPC FEEs provide us with 100 ns
984 long LVDS output signals that are injected into the TDCs' input. V1190A are
985 VME units accepting 128 independent Multi-Hit/Multi-Event TDC channels whose
986 signals are treated by 4 100 ps high performance TDC chips developed by CERN
987 / ECP-MIC Division. Any avalanche signal that gives a signal above the FEEs
988 threshold is thus recorded by the TDCs as a hit within the match window. Each hit
989 is assigned to a specific TDC channel with a time stamp with a precision of 100 ps.
990 The reference time, the 0, is provided by the beginning of the match window. thus

991 for each trigger, coming from a scintillator coincidence or the pulse generator, a
 992 list of hits is stored into the TDCs buffers and will then be transferred into a ROOT
 993 Tree.
 994

995 The v1718 object is defined in the DAQ software as followed.

```

class v1718{

    private :
        int                Handle;

        Data32             Data;           // Data
        CVIRQLevels        Level;          // Interrupt level
        CVAddressModifier AM;              // Addressing Mode
        CVDataWidth        DataSize;       // Data Format
        Data32             BaseAddress;    // Base Address

    public:
        v1718 (IniFile *inifile);
        ~v1718 ();
        long                GetHandle (void) const;
        int                 SetData (Data16 data);
        Data16              GetData (void);
        int                 SetLevel (CVIRQLevels level);
        CVIRQLevels         GetLevel (void);
        int                 SetAM (CVAddressModifier am);
        CVAddressModifier   GetAM (void);
        int                 SetDataSize (CVDataWidth datasize);
        CVDataWidth         GetDataSize (void);
        int                 SetBaseAddress (Data16 baseaddress);
        Data16              GetBaseAddress (void);
        void                CheckStatus (CVMErrorCodes status) const;
        bool                CheckIRQ ();
        void                SetPulsers ();
        void                SendBUSY (BusyLevel level);
};

```

A.2.3 DataReader

997

998

999

1000

1001

1002

1003

1004

1005

1006

1007

1008

1009

1010

1011

1012

1013

1014

```

class DataReader
{
    private:
        bool        StopFlag;
        IniFile *iniFile;
        Data32       MaxTriggers;
        v1718        *VME;
        int          nTDCs;
        v1190a        *TDCs;
        RAWData      TDCData;

    public:
        DataReader();
        virtual ~DataReader();
        void SetIniFile(string inifilename);
        void SetMaxTriggers();
        Data32 GetMaxTriggers();
        void SetVME();
        void SetTDC();
        int GetQFlag(UINT it);
        void Init(string inifilename);
        void FlushBuffer();
        void Update();
        string GetFileName();
        void WriteRunRegistry(string filename);
        void Run();
};

```

The data transfer is done via Block Transfer (BLT). Using BLT allows to transfer a fixed number of events called a *block*. This is used together with an Almost Full Level (AFL) of the TDCs' output buffers. This AFL gives the maximum amount of 32 bits words that can be written in the buffer before an Interrupt Request (IRQ) is generated and seen by the VME Bridge, stopping the data acquisition to transfer the content of each TDC buffers before resuming. The AFL can, at maximum, be of 32735 words (16 bits). This number corresponds to the depth of the output buffer of a TDC. For each trigger, 6 words or more are written into the TDC buffer:

- a **global header** providing information of the event number since the beginning of the data acquisition,
- a **TDC header**,
- the **TDC data** (if any), 1 for each hit recorded during the event, providing the channel and the time stamp associated to the hit,
- a **TDC error** providing error flags,
- a **TDC trailer**,

- 1015 • **a global trigger time tag** that provides the absolute trigger time relatively
1016 to the last reset, and
- 1017 • **a global trailer** providing the total word count in the event.

1018 When the BLT is used, it is easy to understand that the maximum number of
1019 words that have been set as ALF will not be a finite number of events or, at least,
1020 the number of events that would be recorded into the TDC buffers will not be a
1021 multiple of the block size. In the last BLT cycle to transfer data, the number of
1022 events to transfer will most probably be lower than the block size. In that case, the
1023 TDC can add fillers at the end of the block but this option requires to send more
1024 data to the computer and is thus a little slower. Another solution is to finish the
1025 transfer after the last event by sending a bus error that states that the BLT reached
1026 the last event in the pile. This method has been chosen in GIF++.

1028 Due to irradiation, an event in GIF++ can count up to 300 words per TDC. A
1029 limit of 4096 words (12 bits) has been set to generate IRQ which represent from
1030 14 to almost 700 events depending on the average of hits collected per event. Then
1031 the block size has been set to 100 events with enabled bus errors. When an AFL
1032 is reached for one of the TDCs, the VME bridge stops the acquisition at the hard-
1033 ware level by sending a NIM pulse out of one of the 5 programmable outputs to
1034 the VETO of the coincidence module where the trigger signals originate from. As
1035 long as this signal is ON, no trigger reaches the TDCs anymore.

1037 The data is then transferred one TDC at a time into a structure called RAWData
1038 described below.

```
1039 struct RAWData{
    vector<int>          *EventList;
    vector<int>          *NHitsList;
    vector<int>          *QFlagList;
    vector<vector<int> > *ChannelList;
    vector<vector<float> > *TimeStampList;
};
```

1040 Each event is saved into TBranch of a ROOT TTree as 3 integers that represent
1041 the event ID (EventCount), the number of hits read from the TDCs (nHits), the
1042 quality flag that provides information for any problem in the data transfer (qflag),
1043 and 2 lists of nHits elements containing the fired TDC channel (TDCCh) and their
1044 respective time stamps (TDCtS).


```

RAWData TDCData;
TFile *outputFile = new TFile(outputFileName.c_str(), "recreate");
TTree *RAWDataTree = new TTree("RAWData", "RAWData");

int          EventCount = -9;
int          nHits = -8;
int          qflag = -7;
vector<int>   TDCCh;
vector<float> TDCTS;

RAWDataTree->Branch("EventNumber", &EventCount, "EventNumber/I");
RAWDataTree->Branch("number_of_hits", &nHits, "number_of_hits/I");
RAWDataTree->Branch("Quality_flag", &qflag, "Quality_flag/I");
RAWDataTree->Branch("TDC_channel", &TDCCh);
1046 RAWDataTree->Branch("TDC_TimeStamp", &TDCTS);

//...
//Here read the TDC data and place it into TDCData for as long
//as you didn't collect the requested amount of data.
//...

for(UInt i=0; i<TDCData.EventList->size(); i++){
    EventCount = TDCData.EventList->at(i);
    nHits      = TDCData.NHitsList->at(i);
    qflag      = TDCData.QFlagList->at(i);
    TDCCh      = TDCData.ChannelList->at(i);
    TDCTS      = TDCData.TimeStampList->at(i);
    RAWDataTree->Fill();
}

```

1047 A.2.4 DAQ algorithm overview

1048 A.3 Software export

B

1049

1050

Details on the online analysis package

1051

B.1 Introduction

1052

insert text here



1053

1054

1055

Structure of the hybrid simulation software

1056

C.1 Introduction

1057

insert text here...

